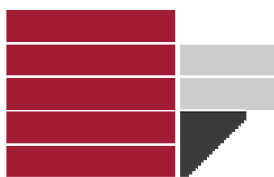


UNIVERSITA' DELLA CALABRIA



Dipartimento di Fisica

**Scuola di Dottorato**

Scuola di Dottorato “Archimede” in Scienze, Comunicazione e Tecnologie

**Indirizzo**

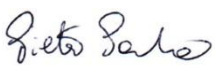
Fisica e Tecnologia Quantistica

**CICLO XXVIII**

***Graphene synthesis by top-down and bottom-up strategies***

**Settore Scientifico Disciplinare : Nanotecnologia**

**Direttore:** Prof. Pietro Pantano

**Firma** 

**Supervisore:** Prof. Lorenzo S. Caputi

**Firma** 

**Supervisore:** Dott.ssa Adalgisa Tavolaro

**Firma** 

**Dottorando:** Dott./ssa Denia M. Cid P.

**Firma** 

**Anno accademico:** 2014 – 2015

Rende-Italia

# Graphene synthesis by top-down and bottom-up strategies

---

## ***ABSTRACT (Italian version)***

Il Grafene è un materiale che ha una struttura bidimensionale composto da atomi di carbonio disposti in una forma esagonale (simile ad un nido d'ape) a formare un film ed ha proprietà fisico-chimiche uniche, tanto che ha suscitato notevole interesse nella comunità scientifica per le sue proprietà e applicazioni. Per produrre Grafene, vengono utilizzati diversi metodi che possono essere divisi in due grandi categorie caratterizzate da un diverso approccio metodologico: l'approccio bottom-up e l'approccio top-down. In questo lavoro, saranno esplorate entrambe le vie.

Questo lavoro di ricerca ha riguardato entrambe le categorie ed in particolare, per quanto riguarda l'approccio bottom-up, saranno riportate le proprietà del grafene su una superficie di nickel monocristallino ottenuto per Deposizione Chimica di Vapori da etilene (CVD).

Nel approccio top-down, la grafite naturale è stata utilizzata per la preparazione di materiali a base di grafene ottenuto per mezzo di una preparazione innovativa.

Tutti i materiali ottenuti sono stati caratterizzati tramite spettroscopia elettronica Auger, Diffrazione di elettroni a bassa energia (LEED), Microscopia elettronica a scansione (SEM) ed a trasmissione (TEM), Spettroscopia Raman, Spettroscopia fotoelettronica a raggi X (XPS) e Spettroscopia di perdita di energia degli elettroni (EELS).

Come risultato, nell'approccio bottom-up, gli atomi di cesio restituiscono la linearità al grafene e questo si comporta come grafene quasi-libero.

Nel approccio top-down, sono stati ottenuti estesi e trasparenti strati di ossido di grafene, privi di difetti. Gli strati preparati chimicamente sono stati ottenuti in forma solida e sembrano coordinare la zeolite ottenendo probabilmente, così, la necessaria stabilizzazione energetica.

## ***ABSTRACT***

Graphene is a two-dimensional structure arranged in a hexagonal form (similar to a honeycomb) that has unique physicochemical properties and has generated interest in the scientific community for its properties and applications. To produce graphene, several methods are used, all of them can be divided in two approaches: the bottom-up approach and top-down approaches. In this work, both routes will be explored.

In the bottom-up approach, the properties of graphene over a mono crystalline nickel surface obtained by chemical vapor deposition (CVD) will be studied.

In the top-down approach, natural graphite will be used to construct graphene based materials with innovative approaches.

Obtained products are characterized by Auger electron spectroscopy, Low energy electron diffraction, Scanning (SEM) and transmission (TEM) electron microscopy, Raman spectroscopy, X-ray photoelectron spectroscopy (XPS) and Energy electron loss spectroscopy (EELS).

As a result, in the bottom-up approach, Cesium restored the linearity of the graphene and it behaved as a free-standing graphene, when is well known that exist a strong interaction between graphene and the metal substrate.

In the top-down approach, graphene oxide free-defect layers that are very large and transparent were obtained. Prepared layers chemically seem to coordinate zeolite crystals probably to obtain the necessary energetic stabilization.

## INDEX

<b><u>ABSTRACT (ITALIAN VERSION) .....</u></b>	<b><u>2</u></b>
--	-----------------

<b><u>ABSTRACT .....</u></b>	<b><u>3</u></b>
------------------------------	-----------------

<b><u>ABBREVIATIONS .....</u></b>	<b><u>6</u></b>
-----------------------------------	-----------------

<b><u>INDEX OF FIGURES .....</u></b>	<b><u>7</u></b>
--------------------------------------	-----------------

<b><u>1. GENERAL PROPERTIES OF GRAPHENE .....</u></b>	<b><u>9</u></b>
---	-----------------

<b>1.1 INTRODUCTION .....</b>	<b>10</b>
<b>1.2 GRAPHENE STRUCTURE.....</b>	<b>11</b>
<b>1.4 HOW TO OBTAIN GRAPHENE.....</b>	<b>14</b>
<b>1.5 EXPERIMENTAL APPARATUS .....</b>	<b>15</b>
<b>1.6 EXPERIMENTAL TECHNIQUES .....</b>	<b>19</b>
1.6.1 LOW-ENERGY ELECTRON DIFFRACTION (LEED): .....	19
1.6.2 AUGER SPECTROSCOPY .....	22
1.6.3 X-RAY PHOTOELECTRON SPECTROSCOPY(XPS).....	23
1.6.4 ELECTRON ENERGY LOSS SPECTROSCOPY (EELS).....	25
1.6.4.1 Introduction.....	25
1.6.4.2 EEL spectrum .....	27
1.6.4.3 EELS theory.....	31
1.6.4.5 EELS in reflection geometry:.....	36
<b>1.7 RESULTS .....</b>	<b>39</b>

<b><u>2. GRAPHENE FROM GRAPHITE: EXFOLIATION AND OXIDATION .....</u></b>	<b><u>45</u></b>
--	------------------

<b>2.1 INTRODUCTION .....</b>	<b>46</b>
<b>2.2 HOW TO OBTAIN GRAPHENE (SECOND PART) .....</b>	<b>47</b>
2.2.1 EXFOLIATION .....	47
2.2.1.1 Mechanical Exfoliation: .....	47
2.2.1.2 Exfoliation in the presence of solvents .....	48
2.2.2 CHEMICAL PREPARATION .....	48
2.2.2.1 Preparation of Graphite Oxide by oxidation .....	48
2.2.2.2 Graphene oxide .....	49
2.2.2.3 GO structure: .....	50
<b>2.3 ZEOLITES.....</b>	<b>52</b>

<b>2.4 EXPERIMENTAL TECHNIQUES</b> .....	<b>54</b>
2.4.1 SCANNING ELECTRON MICROSCOPY (SEM) .....	54
2.4.2 TRANSMISSION ELECTRON MICROSCOPY (TEM) .....	56
2.4.3 RAMAN SPECTROSCOPY .....	57
<b>2.5 RESULTS</b> .....	<b>61</b>
2.5.1 GRAPHITE AND HYDROGEN PEROXIDE( $H_2O_2$ ): .....	61
2.5.2 GRAPHITE WITH HYDROCHLORIC ACID (HCL) AND GRAPHITE WITH NITRIC ACID ( $HNO_3$ ): .....	62
2.5.3 GRAPHITE OXIDE (GRAPHITE AND AQUA REGIA).....	65
2.5.4 OXIDE GRAPHENE WITH ZEOLITE 4A.....	69
<b><u>3 FINAL CONCLUSIONS</u></b> .....	<b>77</b>
<b><u>4 REFERENCES</u></b> .....	<b>79</b>
<b><u>PUBLICATIONS</u></b> .....	<b>84</b>
<b><u>ACKNOWLEDGMENTS</u></b> .....	<b>85</b>

## *Abbreviations*

CVD	Chemical vapor deposition
EELS	Electron energy loss spectroscopy
GO	Oxide graphite
GO+4A	Oxide graphene and zeolite
GR	Graphene
LEED	Low energy electron diffraction
RT	Room temperature
SEM	Scanning electron microscopy
TEM	Transmission electron microscopy
UHV	Ultra-high vacuum
XPS	X-ray photoelectron spectroscopy

## *Index of figures*

Fig. 1 Unit cell of monolayer graphene, a and b are the real space unit vector. [4] .....	12
Fig. 2 Brillouin zone of monolayer graphene[4] .....	13
Fig. 3 Scheme of different forms to obtain graphene .....	15
Fig. 4 Ultra-high vacuum chamber .....	16
Fig. 5 Hemispherical selector .....	18
Fig. 6 Ewald's sphere construction for the case of diffraction from a 2D-lattice. The intersection between Ewald's sphere and reciprocal lattice rods define the allowed diffracted beams. ....	20
Fig. 7 Diagram of the LEED optics .....	21
Fig. 8 LEED used for the experiments on this thesis .....	22
Fig. 9 Schematic representation of an Auger process .....	23
Fig. 10 Electrons mean free path as function of their energies.....	26
Fig. 11 Energy distribution of the electrons emitted by the crystal after the interaction with a primary electrons beam of energy $E_p$ .....	28
Fig. 12 Real and imaginary part of the dielectric function $\epsilon$ (upper side) and real and imaginary part of $1/\epsilon$ (bottom side) for the Drude model. ....	33
Fig. 13 real and imaginary part of the dielectric function $\epsilon$ (upper side) and real and imaginary part of $1/\epsilon$ (bottom side) for the Lorentz model.....	35
Fig. 14 EELS reflection geometry representation .....	36
Fig. 15 VSW HA50 hemispherical spect .....	38
Fig. 16 Auger spectroscopy of graphene over Ni(111) .....	39
Fig. 17 LEED of graphene over Ni(111) .....	40
Fig. 18 EELS spectrum of Graphene on Ni(111) (incidence $45^\circ$ , analyzer $39^\circ$ ), the red spectrum is the above spectrum after the subtraction of Ni(111) clean spectrum.....	41
Fig. 19 Graphene on Ni(111) dispersion curve [21] .....	42
Fig. 21 Scanning transmission electron microscopy(STEM) images of Plasmon contribution of Graphene different layers[22] .....	43
Fig. 20 Cs Auger calibration by using the p(2x2) Cs overlayer on clean Ni(111)[59] .....	43
Fig. 22 Energy loss values of the interface- p-plasmon peak plotted vs q for the Graphene/Ni(111) filled circle and for the Graphene/Cs/Ni(111) system (open circle)[21] .....	44
Fig. 23 Proposed atomic models for Graphene oxide[39] .....	51

Fig. 24 SiO <sub>2</sub> and AlO <sub>2</sub> tetrahedra that forms zeolite.....	52
Fig. 25 Image of zeolite type A took with a Scanning electron microscope (SEM) .....	53
Fig. 26 Scanning Electron Microscope- FEI Quanta 200 Instrument .....	55
Fig. 27 Transmisison Electron Microscopy.....	56
Fig. 29 Thermo Fisher DXR Raman microscope .....	59
Fig. 28 Jablonsky Diagram used for represent Raman and Raleigh scattering:.....	59
Fig. 30 The typical Raman spectrum of bulk graphite and graphene with an incident laser, taken from Ferrari et al, 2006 [5].....	60
Fig. 31. SEM image of graphite and hydrogen peroxide.....	61
Fig. 32 Raman spectrum of graphite with hydrogen peroxide .....	62
Fig. 33 SEM images of a) graphite with nitric acid and b) graphite with hydrochloridric acid.....	63
Fig. 34 Raman spectra of Graphite and graphite with some acids. ....	64
Fig. 35. Distribution of the final product.....	65
Fig. 36 SEM image of top sample graphite and aqua regia. ....	66
Fig. 37 SEM images of the center part of the sample graphite and aqua regia .....	66
Fig. 38 SEM images from the bottom part of the sample. ....	67
Fig. 39 TEM images of graphite with aqua regia.....	67
Fig. 40 Raman spectra of graphite and graphite and aqua regia.....	68
Fig. 41 SEM images of a) GO (Hummer's improved) b) GO+4A after first filtration.....	71
Fig. 42 Raman spectra of GO and GO+4A .....	72
Fig. 43 SEM images of GO+4A after several washes.....	73
Fig. 44 TEM images of GO+4A. ....	74
Fig. 45 Sample prepared for UHV system .....	74
Fig. 46 XPS spectra of the GO+4A sample.....	75
Fig. 47 Electron energy loss spectrum in the transmission mode for a single layer of Graphene Oxide[47].....	76
Fig. 48 EELS spectrum of GO+4A.....	76

# ***1. General properties of Graphene***

## ***1.1 Introduction***

Carbon is one of the best-known elements in nature, and has developed an important role in the development of the human history.

Before 1980, just two allotropic forms of carbon were known, graphite and diamond. In 1980 started the so-called “Carbon revolution” because other allotropes were observed.

In 1985, Fullerenes were observed, their name originate from Buckminster Fuller that predicted the structure, and for the discovery and characterization of  $C_{60}$  H. Kroto and R. Smalley received the Nobel price. In 1991, carbon nanotubes were observed by S. Ijima[1][2].

In 2004, a graphene flake was isolated by Geim and Novoselov for the first time using scotch tape, and for this work they received the Nobel prize in 2010[1], [3].

Graphene is a two-dimensional structure arranged in a hexagonal form (similar to a honeycomb) that has unique physicochemical properties and can be considered as the building block for all the graphitic materials (for example fullerenes= wrapped graphene, nanotubes=rolled graphene )[4][5]. Graphene has generated interest in the scientific community for its properties and applications.

To produce graphene, several method are used, all of them can be divided in two approaches: the bottom-up approach and top-down approach. In the top-down the graphite is used as a raw material to obtain graphene layers, while the bottom-up approach takes isolated atoms mainly coming from de dissociation of hydrocarbons, and arrange them in graphene layers. The last route is very important because high-quality graphene is obtained. In this first chapter, the preparation of graphene by the bottom-up method CVD will be studied.

## 1.2 Graphene structure

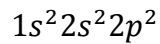
Before to start an intensive study about the applications of graphene, we give a basic review of the properties of carbon.

Carbon has two stable isotopes:

$^{12}\text{C}$  [Nuclear spin :  $I = 0$  ; Nuclear magnetic moment:  $\mu_n = 0$  ]

$^{13}\text{C}$  [Nuclear spin :  $I = \frac{1}{2}$  ; Nuclear magnetic moment:  $\mu_n = 0.7024$  ]

Has six electron and electronic configuration:



with total spin  $s=1$ , orbital moment  $L= 1$  and angular moment  $J= 0$ .

The attractiveness of carbon is its capacity to form various structural forms (called allotropes), this is due to a special electron configuration.

The formation of carbon is tetravalent due to the formation of hybridized states. When carbon promotes one of the 2s electrons into empty orbital 2p<sub>z</sub>, hybrid orbitals are formed.

As it was told before, graphene has a honeycomb crystal lattice. To form graphene, the s, p<sub>x</sub> and p<sub>y</sub> orbitals hybridize, giving rise to orbital  $\sigma$  (occupied) and  $\sigma^*$  (unoccupied) with four electrons, that are distributed two in the orbital s and one in p<sub>x</sub> and p<sub>y</sub> respectively. This electron interacts with other electrons in the same condition and forms strong covalent  $\sigma$  bonds. The p<sub>z</sub> orbital is discordant with respect to planar symmetry and can not interact with  $\sigma$  states, but it interacts with the nearest p<sub>z</sub> orbital creating delocalized  $\pi$  orbital and  $\pi^*$ . The Bravais lattice is triangular, with lattice vectors:

$$\vec{a}_1 = \frac{a}{2}(3, \sqrt{3}) \quad \vec{a}_2 = \frac{a}{2}(3, -\sqrt{3})$$

Where:

$$a \approx 1.42 \text{ \AA}$$

is the nearest neighbor distances (Carbon-Carbon ).

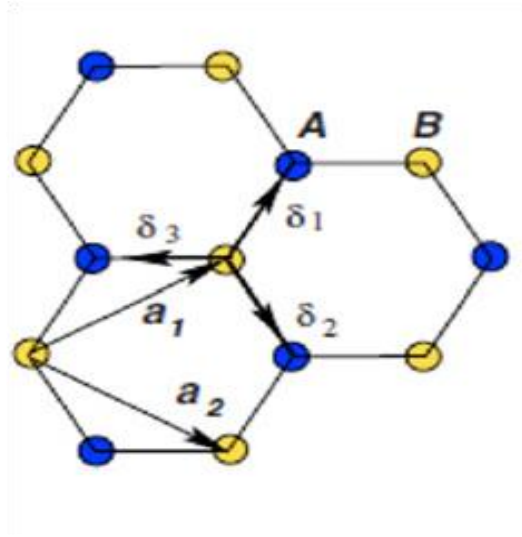


Fig. 1 Unit cell of monolayer graphene,  $a$  and  $b$  are the real space unit vector. [4]

The honeycomb lattice contains two atoms per elementary cell, named A and B (showed in fig.1, they belong to two sublattices), and the reciprocal lattice is also triangular and is described by the unit vectors:

$$\vec{b}_1 = \left( \frac{2\pi}{\sqrt{3}a}, \frac{2\pi}{a} \right) \quad \vec{b}_2 = \left( \frac{2\pi}{\sqrt{3}a}, -\frac{2\pi}{a} \right)$$

corresponding to a lattice constant length  $\frac{4\pi}{\sqrt{3}a}$ . In the Brillouin zone, the points ubicated in the center, the corner and the center of the edge are named  $\Gamma$ ,  $K, K'$  and  $M$ , and are high symmetry points (See: fig 2). And they have wave vectors  $K$ ,  $K'$  and  $M$  that can be expressed mathematically as:

$$\vec{K}' = \left( \frac{2\pi}{3a}, \frac{2\pi}{3\sqrt{3}a} \right)$$

$$\vec{K} = \left( \frac{2\pi}{3a}, -\frac{2\pi}{3\sqrt{3}a} \right)$$

$$\vec{M} = \left( \frac{2\pi}{3a}, 0 \right)$$

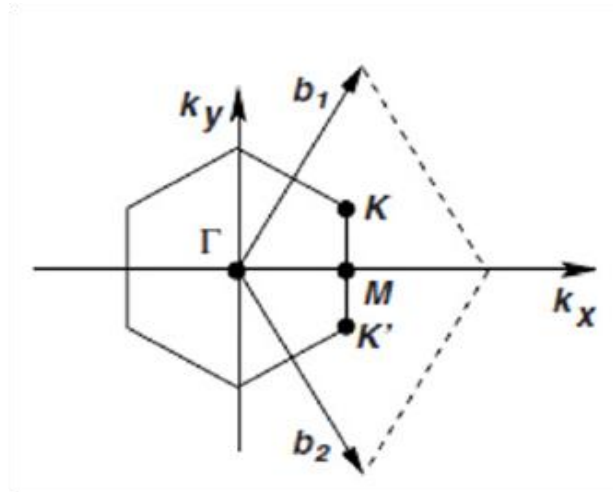


Fig. 2 Brillouin zone of monolayer graphene[4]

Among the more interesting features of the graphene we mention the following:

- Massless Dirac Fermions: One of the major peculiarities of the graphene is that the band structure shows the points in which the bands are linear and intersect at the Fermi level, these areas are called Dirac cones. And for this the electrons behave as massless particles with a speed which is approximately  $c / 300$  (constant velocity even if the energy changes).
- Electron high mobility: electrons have high mobility on graphene, reaching  $10000 \text{ cm}^2 \text{ V}^{-1} \text{ s}^{-1}$  to  $50000 \text{ cm}^2 \text{ V}^{-1} \text{ s}^{-1}$  at room temperature with an intrinsic mobility of  $200000 \text{ cm}^2 \text{ V}^{-1} \text{ s}^{-1}$  [6] [7] but under vacuum; the presence of defects, impurities and number of the layer can hinder the electronic properties of graphene.
- Membrane-like nature: Impermeable to gasses.[4]
- Softness
- Strength: Is the strong material measured with a Young's modulus of  $E=1 \text{ TPa}$  and intrinsic strength of  $130 \text{ GPa}$  in its pristine form[7].

- The thinnest material[8].
- High surface area / mass ratio ( $2600 \text{ m}^2/\text{g}$ ) Has the highest specific surface area of all materials with a theoretical value of  $2630 \text{ m}^2 \text{ g}^{-1}$  and makes it an ideal candidate for a process involving adsorption or surface reactions[6][7].
- Highest thermal conductivity ( $5.3 \times 10^3 \text{ WmK}^{-1}$ )[7]
- Highest electron mean free path at room temperature (about 500 nm).
- Highly transparent (absorbs about 2% in the visible).

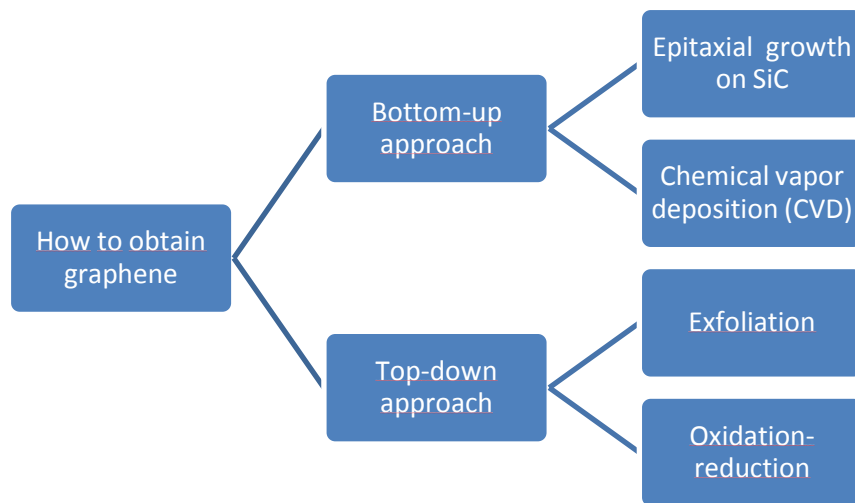
### ***1.4 How to obtain Graphene***

To produce graphene, there are two ways you could choose: bottom-up and top-down approaches.

The bottom-up approach takes the atoms and uses it to construct the desired structures, usually using the CVD technique. In the top-down approach, the graphite is used as a raw material to obtain graphene layers.

Between this two approaches there are several methods for produce graphene as can be seen in Fig.3, more information will be given below.

Fig. 3 Scheme of different forms to obtain graphene



In the epitaxial growth of graphene on SiC, heating the sample results in the sublimation of Si atoms, while C atoms organize spontaneously in an honeycomb graphene layer on the surface[9].

Chemical vapor deposition (CVD) is a process where a substrate is exposed to a hydrocarbon gas (normally ethylene or methane) that decomposes onto the surface leaving adsorbed carbon atoms which, under suitable temperature conditions, can arrange in a graphene layer. Historically, graphitic layers were formed over Ni by exposure to hydrocarbons[1]. The first reported work on graphene layers produced by this method were in 2008 by Q. K. Yu and his group that used Ni[10] as a substrate and X.Li et al that used Cu[11]. This technique has, as advantages that the quality of the samples is extremely high (low defects density), has acceptable lateral dimensions( monolayers of the order of mm) and it is easy to control the thickness.

### ***1.5 Experimental apparatus***

Experiments were carried out at the Surface Nanoscience Laboratory of the Department of Physics of University of Calabria (Unical) in an ultra-high vacuum (UHV) chamber made of stainless steel capable of a base pressure of  $2 \times 10^{-10}$  mbar.

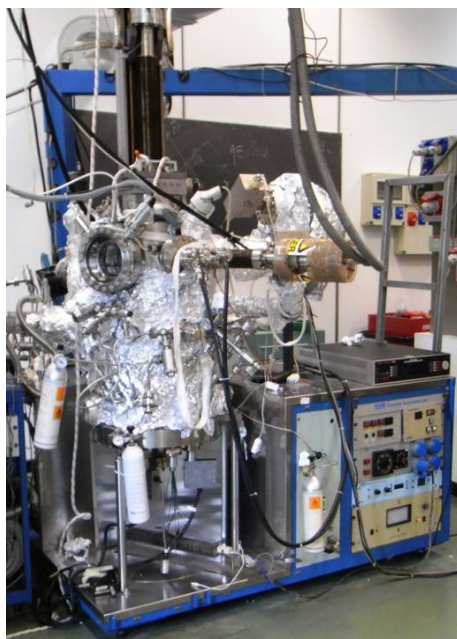


Fig. 4 Ultra-high vacuum chamber

Ultra-high vacuum is the vacuum regime characterized by pressures lower than about  $10^{-9}$  mbar and it is a necessary condition for many surface analytic techniques to reduce surface contamination, by reducing the number of molecules reaching the sample over a given time period. Typically, UHV requires high pumping speed, possibly multiple vacuum pumps in series and/or parallel. The sample inside the vacuum chamber can be translated, rotated and heated by a manipulator. To avoid perturbations to the electron trajectories, all the internal surfaces are grounded, and two  $\mu$ -metal screens inside the chamber limit the intensity of the magnetic field.

The chamber is divided in two sections, which communicate through an hole in the inner  $\mu$ -metal shield. The upper part contains a conventional electron gun that generates an electron beam with energy in the 20-2000 eV range, an X-Ray source which can generate Al and Mg Ka lines, and an hemispherical analyzer to measure energetic spectra of the electron emitted by the sample. In the upper part is also present a Retarding Field Analyzer to study the diffraction of low-energy electrons (LEED), and a gas line to fill the chamber with the desired gases. Also at this level is present an ion gun to clean the surfaces under investigation. At this level it is possible to perform Auger Electron Spectroscopy (AES), X-Ray Photoelectron Spectroscopy (XPS), Low Energy Electron Diffraction (LEED) and conventional Electron Energy Loss Spectroscopy (EELS).

The lower part of the chamber contains an High Resolution Electron Energy Loss (HREELS) spectrometer, made of a fixed monochromator and a rotating analyzer, both based on hemispherical electrostatic analyzer with mean radius of 50 mm.

The monochromator generates a collimated electron beam with energy in the range 0-300 eV. Scattered electrons are analyzed by the rotating analyzer, which has an acceptance angle of  $2^\circ$

### **Ion Gun**

The ion gun consists of a cathode which emits electrons by the thermionic effect, that are accelerated and spiralized to ionize Ar atoms inside the gun. Such ions are then accelerated towards the sample to remove contaminants by the sputtering effect. Such a procedure results not only in the cleaning of the surface, but also in the degradation of the surface order, which is usually recovered by annealing the sample at a suitable temperature, allowing the surface atoms to rearrange in their crystalline lattice.

### **Electron Gun**

The system contains two different electron guns. The one present in the upper part is a conventional gun, in which electrons emitted by an heated filament are accelerated and focused to the sample, to carry out AES and EELS spectroscopies. The gun present in the lower section of the chamber, which is part of the HREELS spectrometer, generates a monochromated electron beam, employed to investigate the electronic and vibrational properties of surfaces. Also in this case, an hot filament emits electron with an energy spread which is unsuitable if we want to distinguish energy loss peaks close in energy, so we need monochromatic electron, with a spread of few meV. The monochromatization is obtained by passing electron in an hemispherical capacitor with radii  $R_1$  and  $R_2$  and through an electrostatic lens system, as shown in fig. 5.

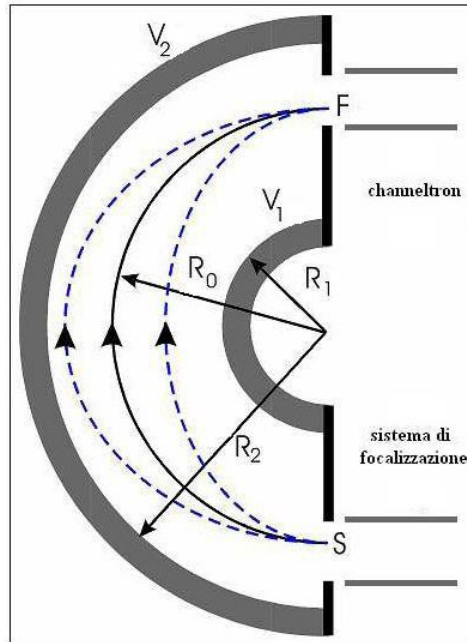


Fig. 5 Hemispherical selector

Different voltages are applied to the hemispheres, so among the electrons entering at S with different energies, only those with energy  $E_{pass}$  will follow a circular path with radius  $R_0 = (R_1 + R_2)/2$ . The pass energy is related to the potential difference between the inner and the outer sphere by the relation

$$E_{pass} = \Delta V \frac{R_1 R_2}{R_1 + R_2}$$

In this way the hemispherical capacitor is able to decrease the energy spread of the electron beam. Of course, the monochromatic beam will have a proper spread, determined by the finite apertures S and F, so the electron beam energy is  $E_{pass} \pm \Delta E$ , which can be considered as an error in the determination of  $E_{pass}$ . The energy spread  $\Delta E$  depends on  $E_{pass}$ , on the width  $d$  of the slits S and F, and on the angular acceptance  $\alpha$  according to the equation

$$\Delta E = E_{pass} \left( \frac{d}{2R_0} + \frac{\alpha^2}{4} \right)$$

After passing through the capacitor, the electron beam is focused on the sample by two planar electrostatic deflectors and by an electrostatic cylindrical optics.

## Electron analyzers

Due to the interaction with impinging electron or X-rays, the sample emits electrons in different directions. Such electrons have to be energy scanned to investigate the properties of the surfaces. The electron analyzers in the upper and in the lower parts of the experimental apparatus consist of hemispherical capacitor similar to that shown in fig. 5. The electron coming from the sample in the solid angle determined by the aperture of the analyzer are focused by an electrostatic optics into the capacitor, and then dispersed by the capacitor depending on their energies. The electrons which follow the right path at the energy  $E_{\text{pass}}$  are then detected at the exit. If this detection is made while scanning the potential difference  $\Delta E$  between the spheres, an energy spectrum is obtained. As mentioned above, lower values of  $E_{\text{pass}}$  implies a lower energy indetermination, so a retarding potential at the entrance of the selector reduces the energy of the incoming electrons down to the  $E_{\text{pass}}$  value. By changing the retarding potential it is possible to scan the energy and intensity of all the electrons, while, maintaining fixed the pass energy value, the instrumental energy indetermination remains constant for the whole spectrum. Moreover the analyzer can rotate around the z axis so it is possible to acquire energy spectra at different angles respect to the normal to the sample.

As for all experimental instruments, increasing of accuracy (low  $E_{\text{pass}}$ ) implies a decreasing in the intensity of signal and vice versa, so a good setting is a good balance between these two conditions.

## 1.6 Experimental techniques

### 1.6.1 Low-energy electron diffraction (LEED):

The Low Energy Electron Diffraction (LEED) is a technique which allow to study the surface long range order of crystalline materials by studying the diffraction of a collimated beam of low energy electrons (20-200 eV). If electrons are represented by plane waves with wavelength in accordance to the de Broglie hypothesis

$$\lambda = \frac{h}{\sqrt{2mE}}, \quad \lambda[\text{nm}] \approx \sqrt{\frac{1.5}{E[\text{eV}]}}$$

it is clear that diffraction will take place if the electron beam energy is in the above range.

The interaction between the incident electrons and the scatters on the surface is conveniently described using the reciprocal lattice of the surface. In three dimensions, the primitive reciprocal lattice vectors are related to the real space vectors  $\mathbf{a}$ ,  $\mathbf{b}$  and  $\mathbf{c}$  in the following way:

$$\mathbf{a}^* = \frac{2\pi \mathbf{b} \times \mathbf{c}}{\mathbf{a} \cdot (\mathbf{b} \times \mathbf{c})}, \quad \mathbf{b}^* = \frac{2\pi \mathbf{c} \times \mathbf{a}}{\mathbf{b} \cdot (\mathbf{c} \times \mathbf{a})}, \quad \mathbf{c}^* = \frac{2\pi \mathbf{a} \times \mathbf{b}}{\mathbf{c} \cdot (\mathbf{a} \times \mathbf{b})}$$

For an incident electron with wave vector  $k = \frac{2\pi}{\lambda_0}$ , the condition for constructive interference and hence for diffraction is given by the Laue condition

$$k - k_0 = G_{hkl}$$

Where  $k = \frac{2\pi}{\lambda}$  is the scattered wavevector and  $G_{hkl} = ha^* + kb^* + lc^*$  is a vector of the reciprocal lattice, with (h,h,l) a set of integers. The magnitude of the wavevectors  $k$  and  $k_0$  is the same, because only elastic scattering is considered. In two dimensions, the Laue condition reduces to the form

$$k \parallel -k_0 \parallel = G_{hkl} = ha^* + kb^*,$$

where  $a^*$  and  $b^*$  are the primitive translations vectors of the two-dimensional reciprocal lattice of the surface, and  $k \parallel$  and  $k_0 \parallel$  denote the component parallel to the surface of the reflected and incident electrons respectively.

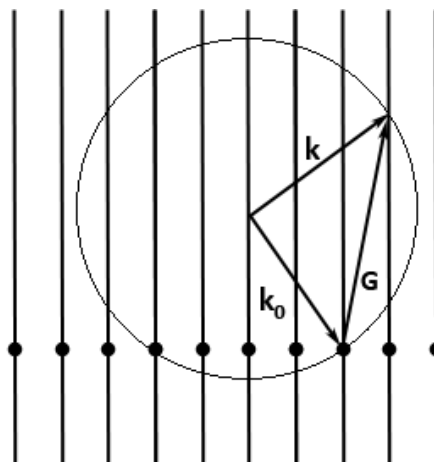


Fig. 6 Ewald's sphere construction for the case of diffraction from a 2D-lattice. The intersection between Ewald's sphere and reciprocal lattice rods define the allowed diffracted beams.

Elastically reflected electrons are revealed by a retarding field analyzer (RFA) with an integrated electron gun, as schematically shown in fig. 7.

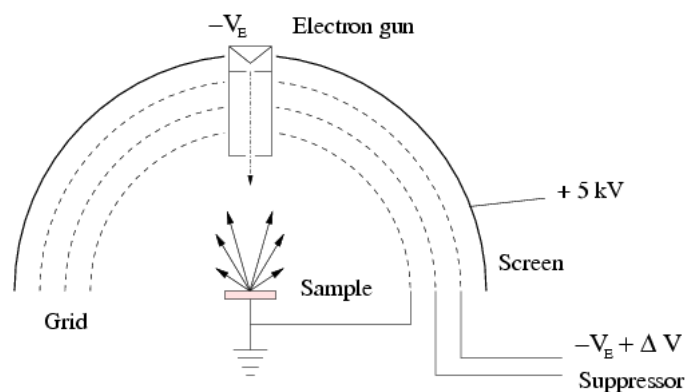


Fig. 7 Diagram of the LEED optics

The electron gun can produce electron which are accelerated and focused into a beam, typically about 0.1 to 0.5 mm wide, by a series of electrodes serving as electron lenses beams. with the energy of 20-200 eV. Some of the electrons incident on the sample surface are backscattered elastically, and diffraction can be detected if sufficient order exists on the surface. A series of metallic grids (three or four) are used for screening out the inelastically scattered electrons; the first grid screens the space above the sample from the retarding field, the next grid is at a potential to block low energy electrons and is called the suppressor. Only the elastically scattered electrons are accelerated and hit a fluorescent screen producing on the screen the projecting of the reciprocal lattice of the sample. The screen usually is located on the wall of the vacuum chamber and it's possible to observe the diffraction LEED pattern from the outside. By looking at fig. 6, it is clear that the image observed on the fluorescent screen is a direct picture of the surface reciprocal lattice.



Fig. 8 LEED used for the experiments on this thesis

### 1.6.2 Auger spectroscopy

Auger spectroscopy measures the kinetic energy of the emitted electrons, determines the composition of materials depending on the depth, film growth and cleanliness in the surface.

In 1920, Klein and Roseland observed the relaxation of an excited atom can be obtained through photon or electron emission and this is the physical process that forms the base of Auger spectroscopy. In 1923, P. Auger found that the energy of the emitted electrons was independent of the frequency of the primary X-ray beam and the electron energy was characteristic for each element. The first AES surface analysis was performed by Lander in 1953 using UHV.

Auger effect happens when a vacancy in an inner shell of an atom is created. After that, the vacancy is occupied by an electron from a higher energy level, and the emitted energy is transmitted to a third electron that leaves the crystal with an energy KE that mathematically can be represented as

$$KE = E_A - E_B - E_C$$

Where

$E_A$  is the energy of the atom with a vacancy

$E_B$  is the energy of the energetic level in at which is the second electron

$E_C$  Is the energy of the electron that leaves the crystal.

Auger Electrons are classified in the base at the energetic levels that participate in the process.

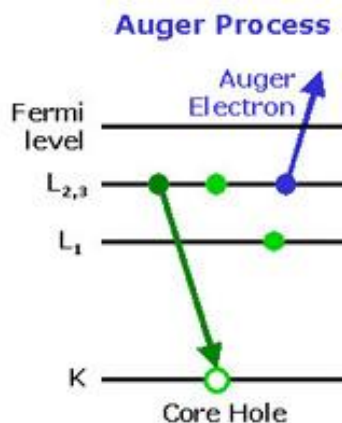


Fig. 9 Schematic representation of an Auger process

One of the advantages of this technique is the ability to analyze just a fragment of the surface, the limitation of this technique is that the samples must be solid. Because its high sensitivity was used for appreciating crystal growth and monitor during cleaning surfaces of samples, detecting impurities in the surface and interface.

Is a useful complement to LEED because Auger electron comes from about the same depth making possible the analysis of the region that determinates the diffraction pattern[12].

When AES is combined with EELS is easy to obtain information about the bulk composition and bonding.

### ***1.6.3 X-ray Photoelectron spectroscopy(XPS)***

XPS consists in irradiating a surface with monoenergetic soft X-rays and in analyzing in energy the photoelectrons emitted. Each element of the periodic table has a unique spectrum, related to the binding energies of its electronic energy levels. The spectrum from a mixture of elements is approximately the sum of the spectra of the single constituents. Because photoelectrons have small mean free paths, XPS is a surface-sensitive technique. Quantitative measurements of surface atomic concentrations can be obtained by peak heights or peak areas, and the high resolution determination of the peak positions can allow the identification of chemical states. A conventional XPS system is made of a source of X-rays, based on the emission of X-rays from a magnesium or

aluminum anode bombarded by electrons with energy of the order of some keV. Non-monochromatic magnesium X-rays have a wavelength of 9.89 angstroms which corresponds to a photon energy of 1253 eV. The energy width of the non-monochromatic X-ray is roughly 0.70 eV, which, in effect is the ultimate energy resolution of a system using non-monochromatic X-rays. The energy of the photoelectrons depends on the photon energy according to the following equation:

$$K = h\nu - E_b - \Phi$$

where K is the kinetic energy of the detected electron,  $h\nu$  is the energy of the incident photon,  $E_b$  is the binding energy of the involved atomic orbital, and  $\Phi$  is the analyzer work function. The binding energy  $E_b$  is a characteristic of a specific element, in fact, usually, the XPS spectra are represented as function of the binding energy ( $E_b = h\nu - K - \Phi$ ) and each peak of these spectra can be used to identify the presence of the element that has a unique set of binding energies. As said above, in addition to photoelectrons emitted in the photoelectric process, Auger electrons may be emitted because of relaxation of the excited ions remaining after photoemission. The Auger peaks energy (EA) are independent from the photon incident energy, so in the binding energy representation of XPS measurements, the Auger energies are given by:

$$E_A^{bind} = (h\nu - \Phi) - E_A$$

For many XPS investigations, it is important to determine the relative concentrations of the various constituents. Methods have been developed for quantifying the XPS measurement utilizing peak area and peak sensitivity factors. This approach is satisfactory for quantitative work. For a sample that is homogeneous in the analysis volume, the number of photoelectrons per second in a specific spectra peak is given by:

$$I = nf\sigma\theta y\lambda AT$$

where n is the number of atoms of the element per  $\text{cm}^3$  of the sample, f is the x-ray flux,  $\sigma$  is the photoelectric cross section for the atomic orbital of interest,  $\theta$  is an angular efficiency factor for the instrumental arrangement based on the angle between the photon path and detected electron,  $y$  is the efficiency in the photoelectric process for formation of photoelectrons of the normal photoelectron energy,  $\lambda$  is the mean free path of the photoelectron in the sample, A is the area of the sample from which photoelectrons are detected and T is the detection efficiency for electrons emitted from the sample. From previous expression we obtain

$$n = \frac{I}{f\sigma\theta y\lambda AT}$$

and the denominator can be defined as the atomic sensitivity factor S. If we consider a strong line from each of two elements, then  $\frac{n_1}{n_2} = \frac{I_1/S_1}{I_2/S_2}$ . Therefore, a general expression for determining the atom fraction of any constituent in a sample,  $C_x$ , can be written as an extension of previous equation

$$C_x = \frac{n_x}{\sum n_i} = \frac{I_x/S_x}{\sum I_i/S_i}$$

For transition metal spectra it is best to include the entire 2p region when measuring peak area. It has to be noted that an overlying contamination layer can affect this quantitative analysis, because atoms placed only on the surface have the effect of modifying the intensity of electrons coming from underlying layers, diminishing the intensity of high binding energy peaks more than that of low binding energy peaks.

## ***1.6.4 Electron energy loss spectroscopy (EELS)***

### ***1.6.4.1 Introduction***

Electron Energy Loss Spectroscopy (EELS) is used to investigate the excitations in a crystal, caused by an incident electrons beam called primary beam, by analyzing the energy spectrum of electrons backscattered from the surface. Primary electrons can interact with electron clouds of the sample and transfer some of its kinetic energy to them. There are two kinds of EELS, they are:

1. Electron Energy Loss Spectroscopy (EELS)
2. High Resolution Electron Energy Loss Spectroscopy (HREELS)

EELS uses electrons from 0.1 to 10 keV originating from a conventional electron gun. The incident electrons beam interacts with the surface of the material of interest and the reflected beam contains inelastically scattered electrons whose energy is decreased by amounts corresponding to

characteristic absorption energies in the solid. Bulk and surface plasmons are the principal features of these spectra.

HREELS - The high resolution energy in the incident beam is achieved by monochromatizing a thermionic electron beam. The incident electrons are of quite low energy (a few eV) and the losses are in the meV range. This technique allows to study in detail the low-energy plasmons, the phonons and the vibrational properties of adsorbates. As such, it is a competitive technique with Reflection Absorption Infra Red Spectroscopy (RAIRS). RAIRS has the advantage of significantly greater energy resolution, but HREELS can study vibrational features of energy right down to a few meV (depending upon the width of the incident beam). The energy of the primary beam has fundamental importance to understand how deep the sample is probed. The figure 10 represents the mean free path (counted in monolayers) versus the energy of the incident electron beam.

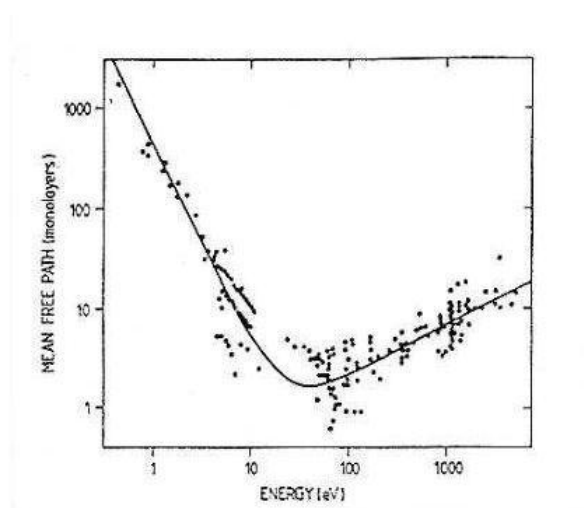


Fig. 10 Electrons mean free path as function of their energies

The mean free path, that is the mean distance covered by an electron in a medium before to undergo an inelastic collision, shows a minimum around 50 eV, and after this minimum, increasing primary energy implies the increasing of the mean free path. This graph is universal, it means that it's a good estimate of electrons mean free path in all media, and also shows that to probe more than 10 monolayers (10-20 Å) of materials it's necessary to use electrons of more than 1000 eV of energy. Therefore, all our HREELS measurements, carried out at a primary energy of about 100 eV, carry informations mainly coming from the first atomic layers of the sample.

### 1.6.4.2 EEL spectrum

In electron energy-loss spectroscopy, we deal directly with the *primary* process of electron excitation, in which primary electrons undergo losses of different amounts of energy. A portion of the primary electrons scattered by the sample are analyzed by the high-resolution electron spectrometer, that separates the electrons according to their kinetic energy and produces an *electron energy-loss spectrum* showing the number of electrons (scattered intensity) as a function of their decrease in kinetic energy.

Many of the scattered electrons have almost the same energy of the incident electron beam (elastic peak), while some electrons are emitted with lower energy with respect to the primary energy. These latter are inelastic electrons and the energy they lost ( $E_{loss}$ ) is the same energy that the crystal absorbed to produce an excitation.

The sample excitations induced by an electronic perturbation, are mainly divided into three groups, each for a specific energy range:

1. Core electron excitations ( $E_{loss}$  of the order of hundreds of eV)
2. Valence band excitations (single particle interband or intraband transitions), surface and bulk collective excitations (plasmons) ( $E_{loss}$  of the order of tens of eV)
3. Vibrational excitations of the sample (acoustic and optic phonon) and vibrational excitations of atoms or molecules adsorbed on the surface ( $E_{loss}$  of the order of meV)

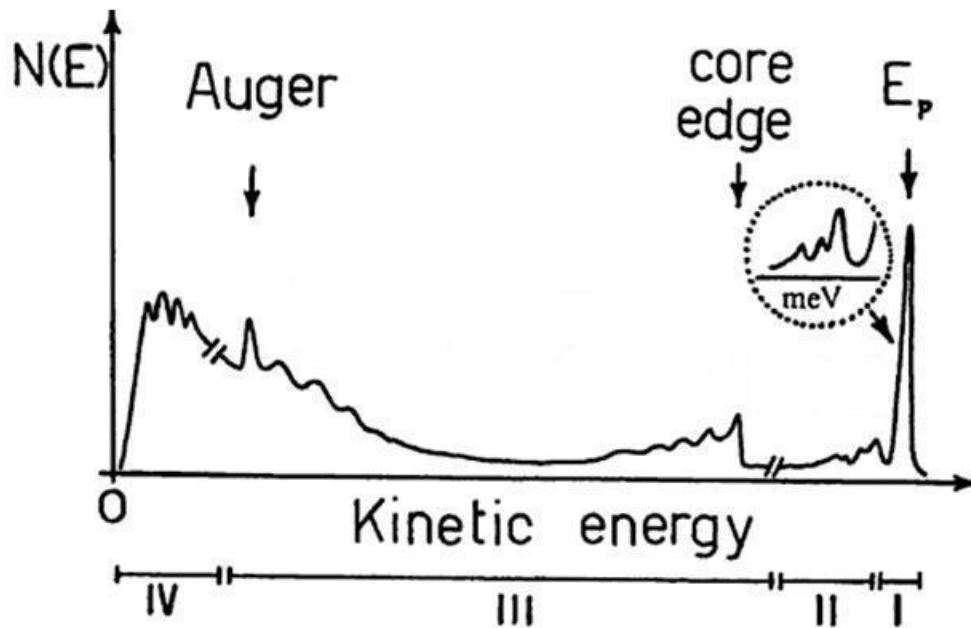


Fig. 11 Energy distribution of the electrons emitted by the crystal after the interaction with a primary electrons beam of energy  $E_p$

In the previous graph is plotted the general energy distribution  $N(E)$  of the electrons emitted by the crystal as a result of the interaction with a primary electrons beam of energy  $E_p$ . The graph can be divided in four sections, representing different ranges of  $E_{loss}$  with different sample information:

The region I includes the highest peak of the energy distribution with energy  $E_p$  that is the elastic peak and allows finding information about the structure of the sample. It contains all electrons that are reflected by the specimen with an elastic interaction only. In the vicinity of the elastic peak, there are vibrational excitations which can be determined only by the high resolution EELS (HREELS). By means of these losses it is possible to obtain information about the vibrational modes of the crystal (phonons) and the vibrational excitations of atoms and molecules adsorbed on the surface.

In the second region (II) it is possible to distinguish all the electrons that had inelastic interaction with the solid. The EELS spectroscopy is used, in this energy range, to have information about surface and bulk collective excitations and also about its dielectric function. Here, the plasmon peaks are the predominant features.

In the third region (III) are electrons which suffered higher energy losses, and secondary electrons at high energy. In this energy range can be found Auger electrons and core electron excitations. As in an X-ray spectrum there are additional peaks at well-defined sites in the EELS above the background. These ionization edges appear at electron energy losses that are again typical for a specific element and thus qualitative analysis of a material is possible by EELS. The onset of such ionization edges correspond to the threshold energies that are necessary to promote inner shell electrons from their energetically favored ground state to the lowest unoccupied levels. These energies are specific of the shell and of the element. Above this threshold energy, all energy losses are possible since an electron transferred to the vacuum might carry any amount of additional energy. If the atom has a well-structured density of states (DOS) around the Fermi level, not all transitions are equally likely. This gives rise to a fine structure of the area close to the edge that reflects the DOS and gives information about the bonding state. This method is called electron energy loss near edge structure (ELNES). From a careful evaluation of the fine structure farther away from the edge, until hundreds eV above the core excitations, information about coordination and interatomic distances are obtainable (extended energy loss fine structure, EXELFS).

The last region (IV) contains an high and wide peak caused by the secondary electrons, also this peak has a fine structure that can be analyzed by the angle-resolved Secondary Electron Emission (SEE). This analysis provides information about the density and the dispersion of empty states just above the Fermi level.

There are several basic ways to perform EELS, primarily classified by the geometry and by the kinetic energy of the incident electrons. Probably the most common today is transmission EELS, in which the kinetic energies are typically 100 to 300 keV and the incident electrons pass through the material sample. Usually this occurs in a transmission electron microscope (TEM), although some dedicated systems exist which enable extreme resolution in terms of energy and momentum transfer at the expense of spatial resolution.

The transmission EELS can be used on very thin sample, because the analyzer acquires the electron beam that passes through the material (transmitted beam) and from this analysis it's possible to extract proprieties about the bulk of the sample. The first reports of this spectroscopy was about the transmission geometry and it was used a primary beam of (50-200 KeV) on thin samples [13]–[16]. Instead, the reflection geometry is particularly sensitive to surface properties but is limited to very small energy losses such as those associated with surface plasmons or direct interband transitions. Lucas et al [17] made the first publications about this, followed by Evans[18], [19] and Mills[20].

The EELS spectroscopy has several analogies with the optic one, in fact both techniques give information about the density of electronic states in the examined solid. EELS, however, makes it possible to change easily the energy of the incident beam, in order to probe a larger energy range. Furthermore, the low mean free path of electrons in the reflection geometry makes this technique more sensible to the surface proprieties with respect to optical spectroscopy.

### 1.6.4.3 EELS theory

In a continuous and homogeneous medium, the response to an electric external perturbation can be described by the dielectric theory. When an electron approaches a dielectric material, the electrons density inside the solid changes to shield the long range electric field produced by the incoming perturbation. The density fluctuations generated inside the medium are related to the wave vector and the frequency of the external field, so the transferred energy depends on the field density energy variation inside the solid.

An electron inside the solid can acquire energy  $\hbar\omega$  and impulse  $\hbar\mathbf{q}$ , because of inelastic interaction with an incident electron, if it lost the same amount of energy  $\Delta E = \hbar\omega$ .

The incident electron can be described by the electronic distribution:

$$\rho(\mathbf{r}, t) = -e \delta(\mathbf{r} - \mathbf{v}t)$$

The interaction potential produced inside the solid follows the Poisson equation:

$$\varepsilon(\mathbf{q}, \omega) \nabla^2 \varphi(\mathbf{r}, t) = -4\pi \delta(\mathbf{r} - \mathbf{v}t)$$

If we pass in the Fourier space, the transform function of  $\varphi(\mathbf{r}, t)$  is:

$$\varphi(\mathbf{q}, \omega) = \frac{8\pi^2 e}{q^2 \varepsilon(\mathbf{q}, \omega)}$$

The energy loss of the electron in length unit inside the medium is  $E_x|_{r=vt}$ , where  $E_x$  is the component of the electric field along the x axis, perpendicular to the surface.

Whereas

$$E(\mathbf{r}, t) = -\nabla\varphi(\mathbf{r}, t) = -i \int \mathbf{q} dq \int d\omega \varphi(\mathbf{q}, \omega) e^{i(\mathbf{q}\cdot\mathbf{r}-\omega t)}$$

Replacing in this equation, the expression found for  $\varphi(\mathbf{r}, t)$  we obtain the loss energy probability in length unit as function of the exchanged moment  $\mathbf{q}$  and of the frequency  $\omega$ :

Where

$$-Im\left[\frac{1}{\varepsilon(\mathbf{q}, \omega)}\right] = \frac{\varepsilon_2}{\varepsilon_1^2 + \varepsilon_2^2}$$

is the bulk loss function.

So the bulk loss function describes the inelastic interaction of high energy electrons that pass through the sample.

A maximum in the loss function occurs when  $\varepsilon_1 = 0$  and  $\varepsilon_2 \approx 0$ . One can see the large oscillations and response will occur if  $\varepsilon_1 = 0$ , which takes place at the plasma frequency.

The most used models to describe a solid material are the Drude and Lorentz models. The first one deals the conduction electrons as a free electrons gas not subject to atomic potential, and in this case the dielectric function, in the limit of  $q \rightarrow 0$ , is:

$$\varepsilon(\omega) = 1 - \frac{\omega_p^2}{\omega^2 + i(\omega/\tau)}$$

where  $\omega_p$  is the plasma frequency ( $\omega_p^2 = \frac{4\pi n e^2}{m_e}$ ) and  $\tau$  is the relaxing time that takes into account the interactions between the electrons.

In the following graph are represented the real and the imaginary part of  $\varepsilon$  and  $-Im[1/\varepsilon]$ :

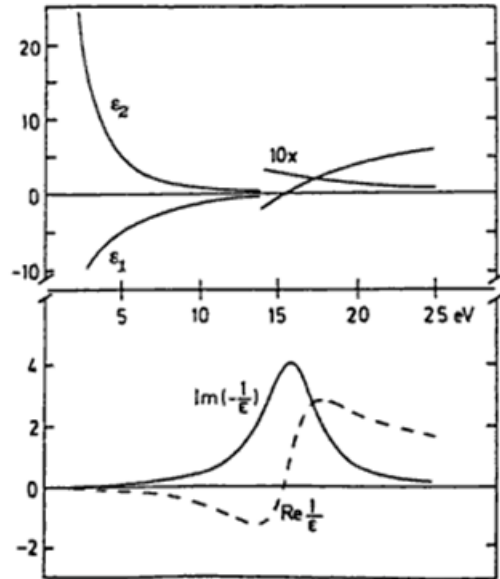


Fig. 12 Real and imaginary part of the dielectric function  $\epsilon$  (upper side) and real and imaginary part of  $1/\epsilon$  (bottom side) for the Drude model.

The imaginary part of the dielectric function,  $\epsilon_2$  is monotonically decreasing and does not exhibit any structure, so a free electron gas does not generate any optical absorption. The loss function, instead, exhibits a maximum at the plasma frequency  $\omega_p$ , corresponding to the excitation energy of a bulk plasmon in a free electron gas (from several eV to few tens of eV).

Lorentz model is based on treating electrons as damped harmonically bound particles subject to external electric fields. This model describes successfully bound electrons in a solid interacting with an electric field  $\mathbf{E}$  and affected by an elastic-like restoring force with a own resonance frequency  $\omega_0$ . Furthermore, to adapt, this ideal model to the experimental reality, the existence of a viscous term  $\Gamma$  is assumed that can explain the linewidths experimentally observed and avoid annoying divergences. The real materials have different resonances with different intensities, so it is associated at the resonance frequency  $\omega_0$ , an empirical parameter  $f_0$  called oscillator strength factor through which it possible to weigh the different intensities, so it satisfies the relation:

$$\sum_i f_i = 1$$

To obtain the Lorentz oscillator relation, in the single resonance frequency  $\omega_0$  case, we start from the second law of dynamics:

$$m(\ddot{x} + \Gamma\dot{x} + \omega_0^2x) = eE$$

Where  $m$  is the electron mass,  $e$  is the electron charge and  $E$  is the electron external field applied to the material. Solving the equation for  $x$  and replacing the external field by  $\mathbf{E} = \mathbf{E}_0 e^{-i\omega t}$ , it is obtained:

$$\mathbf{x} = \frac{\left( \frac{e\mathbf{E}_0}{m} \right) e^{-i\omega t}}{\omega_0^2 - \omega^2 - i\omega\Gamma}$$

Using the equations for the microscopic dipole  $\mathbf{p} = e\mathbf{x}$  and for macroscopic polarization  $\mathbf{P} = n\mathbf{p}f_0$  it is extracted:

$$\mathbf{P} = \frac{\left( \frac{ne^2}{m} \right) f_0 \mathbf{E}_0 e^{-i\omega t}}{\omega_0^2 - \omega^2 - i\omega\Gamma}$$

Knowing that polarization and electric field are related through the equation  $\mathbf{P} = \varepsilon_0(\varepsilon - 1)\mathbf{E}$  the dielectric function, for just one type of transition  $\hbar\omega_0$  is

$$\varepsilon(\omega) = 1 + \frac{f_0 \omega_p^2}{\omega_0^2 - \omega^2 - i\omega\Gamma}$$

Where  $\omega_p = \sqrt{\frac{ne^2}{m\varepsilon_0}}$  is the plasma frequency and  $f_0$  is the oscillator strength factor.

So for different resonances the real and imaginary part of the dielectric function, respectively  $\varepsilon_1$  and  $\varepsilon_2$ , are:

$$\varepsilon_1(\omega) = 1 + \omega_p^2 \sum_i \frac{f_i(\omega_i^2 - \omega^2)}{(\omega_i^2 - \omega^2)^2 + \omega^2\Gamma_i^2}$$

$$\varepsilon_2(\omega) = \omega_p^2 \omega \sum_i \frac{f_i\Gamma_i}{(\omega_i^2 - \omega^2)^2 + \omega^2\Gamma_i^2}$$

Generally this is a good approximation for semiconductor, insulators and for all metals which possess bound electrons ( $d$  or  $p$  valence electrons).

The following graph reports  $\varepsilon_1$ ,  $\varepsilon_2$ ,  $-Im[1/\varepsilon]$  and  $Re[1/\varepsilon]$  calculated for the Lorentz model

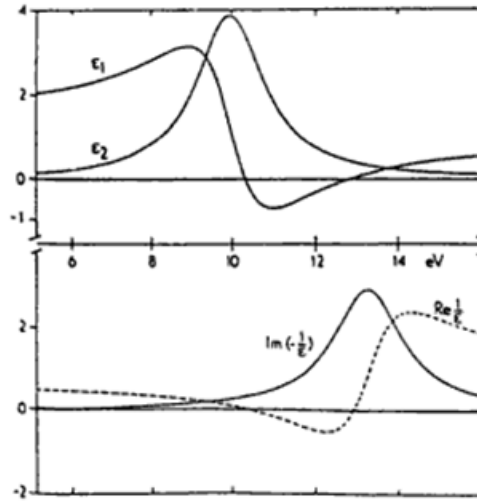


Fig. 13 real and imaginary part of the dielectric function  $\epsilon$  (upper side) and real and imaginary part of  $1/\epsilon$  (bottom side) for the Lorentz model.

The peak in  $\epsilon_2$  function represents an optical absorption at  $\hbar\omega_0$ , while the loss function exhibits a maximum at a frequency  $\omega > \omega_0$  where  $\epsilon_1 = 0$  and  $\epsilon_2 \approx 0$ . The occurrence of these conditions corresponds to a collective excitation in the solid known as “interband plasmon” in analogy to the free electron model.

More generally the behavior of metals is described by a dielectric function that is the sum of the intraband type (Drude model) and the interband type (Lorentz model). So the dielectric function is described by:

$$\begin{aligned}\epsilon_1^{tot}(\omega) &= \epsilon_1^{free}(\omega) + \epsilon_1^{bound}(\omega) \\ \epsilon_2^{tot}(\omega) &= \epsilon_2^{free}(\omega) + \epsilon_2^{bound}(\omega)\end{aligned}$$

Observing trends of  $\epsilon_2$  and  $-Im[1/\epsilon]$  for metals and semiconductors, it's clear that the maximum of these two function are never in the same energy position, on the contrary we can assume that the maximum of  $\epsilon_2$  matches with the minimum of  $-Im[1/\epsilon]$ , like if

$$-Im[1/\epsilon] \sim 1/\epsilon_2.$$

In conclusion this is the evidence that the single particle excitations and the collective excitations are generally in competition, making the EEL probability, in the range of 1-20 eV, inversely proportional to the optical absorption.

### 1.6.4.5 EELS in reflection geometry:

The schematic representation of the EELS in reflection geometry is shown in the following image:

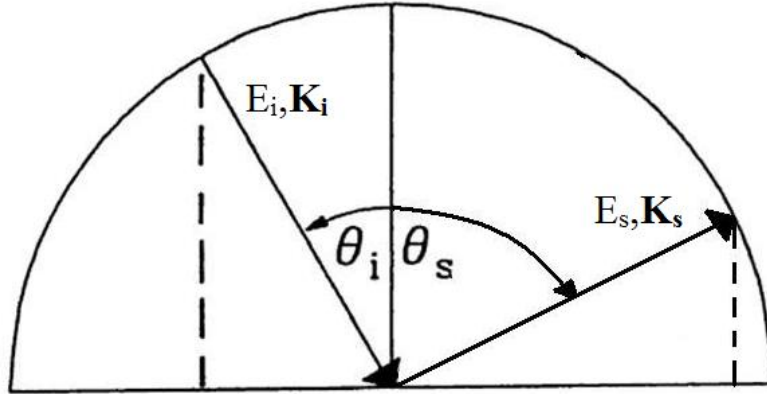


Fig. 14 EELS reflection geometry representation

We assume that an electron with energy  $E_i$  and wave vector  $\mathbf{K}_i$  hits the sample at an angle of incidence  $\theta_i$  with respect to the surface normal and it scatters off the crystal with energy  $E_s$  and wave vector  $\mathbf{K}_s$  at an angle  $\theta_s$ .

We are describing an inelastic process, so the incident electron can transfer energy ( $E_{Loss}$ ) and momentum ( $\mathbf{q}$ ) to the sample. From the conservation rule of energy we know that:

$$E_i = E_s + E_{Loss}$$

The conservation of the component parallel to the surface of the momentum is more restrictive, in fact just the component parallel to the surface must be preserved.

So, for the momentum we have:

$$K_{i\parallel} = K_{s\parallel} + q_{\parallel}$$

Therefore, the component parallel to the surface of the momentum transfer is calculated as

$$|q_{\parallel}| = |\mathbf{K}_i| \sin \theta_i - |\mathbf{K}_s| \sin \theta_s$$

Taking into account the relation between the energy and the momentum for a free electron

$$E = \frac{\hbar^2 K^2}{2m} \text{ we can calculate } |q_{\parallel}|:$$

$$|\mathbf{q}_{\parallel}| = \sqrt{\frac{2m}{\hbar}} (\sqrt{E_i} \sin \theta_i - \sqrt{E_i - E_{Loss}} \sin \theta_s)$$

Thus, using monochromatic electron beam with a rotating analyzer it is possible, for each loss energy, calculate the component parallel to the surface of the momentum transfer obtaining the energy dispersion curve of the observed loss  $\omega(\mathbf{q}_{\parallel})$ .

In the case of a 3D material, the dispersion curve shows a quadratic dependence on the  $q$  momentum.

More precisely for a bulk plasmon described by the Drude model:

$$\omega(q) = \omega_p \left( 1 + \frac{3q^2 v_f^2}{10\omega_p^2} \right)$$

The bulk loss function,  $-Im[1/\epsilon]$ , found above for EELS in transmission geometry, cannot explain surface excitations treated by Mills theory[9]. For what concern electron energy loss spectroscopy in reflection geometry, we should consider the solid as a semi-infinite dielectric half-space in  $z \leq 0$ . In semi-infinite medium, Mills theory ascribes the inelastic diffusion process at the surface to electron density fluctuations induced by an incident electron on a semi-infinite materials. The loss probability function becomes proportional to:

$$-Im \left[ \frac{1}{\epsilon(\mathbf{q}, \omega) + 1} \right] = \left\{ \frac{\epsilon_2(\mathbf{q}, \omega)}{[\epsilon_1(\mathbf{q}, \omega) + 1]^2 + \epsilon_2^2(\mathbf{q}, \omega)} \right\}$$

called surface loss function.

The collective surface excitation lies at the interface between the sample and the vacuum, and the vacuum dielectric constant must be taken into account. For this reason we found “+1” at the denominator. In this case the loss probability has a pole at  $\epsilon_1 + 1 = 0$  and  $\epsilon_2 \approx 0$ . These conditions corresponds to the excitation of a surface plasmon excitation.

We can handle this process with the same theoretical concepts used for the EELS theory in transmission geometry, resulting the surface plasma frequency at:

$$\omega_s = \frac{\omega_p}{\sqrt{2}}$$

It must be noted that the excitation frequency of a surface plasmon is closely connected to its counterpart in volume.

Others maxima in the loss function are in correspondence of  $\varepsilon_2$  peaks, displaced by a factor

$$\frac{1}{(\varepsilon_1 + 1)^2}.$$

A surface plasmon can be understood as a crystal mode which propagates on the surface and is greatly attenuated in the direction perpendicular to it. Generally, EELS investigations in reflection geometry are a linear combination of both loss functions (bulk and surface ones) and the proportionality coefficients depends on the primary beam energy and experimental conditions.



Fig. 15 VSW HA50 hemispherical spect

## 1.7 Results

The Ni(111) was cleaned by repeated cycles of sputtering with 2 keV Ar ions and annealing at 1000K, until a sharp LEED pattern and the Auger spectrum showed a clean and ordered surface.

To grow graphene over Ni (111), UHV chamber worked with a base pressure of  $2 \times 10^{-10}$  mbar. The sample was held at a temperature of 750 K and was exposed to 1000 L ( $1L=10^{-6}$  mbar) of ethylene ( $C_2H_4$ ) at  $10^{-6}$  mbar partial pressure.

After the finalization of this process, Auger spectroscopy was used for its high sensitivity to the chemical composition of the sample and was observed that carbon was deposited in its graphitic form (See Fig. 16).

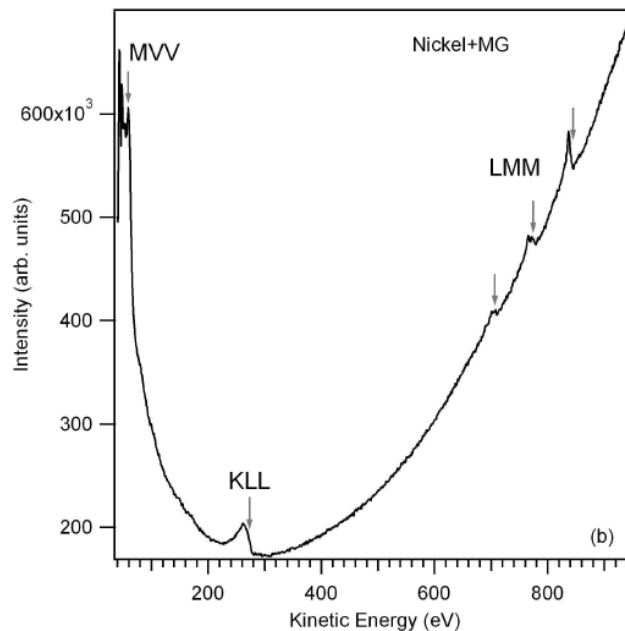


Fig. 16 Auger spectroscopy of graphene over Ni(111)

Low-energy electron diffraction (LEED) was used to observe the reciprocal lattice of graphene over nickel, with the result that the graphene is indistinguishable from the nickel substrate because they have similar reticular parameters, at this situation, could be said that graphene is in perfect register with nickel (fig. 17).

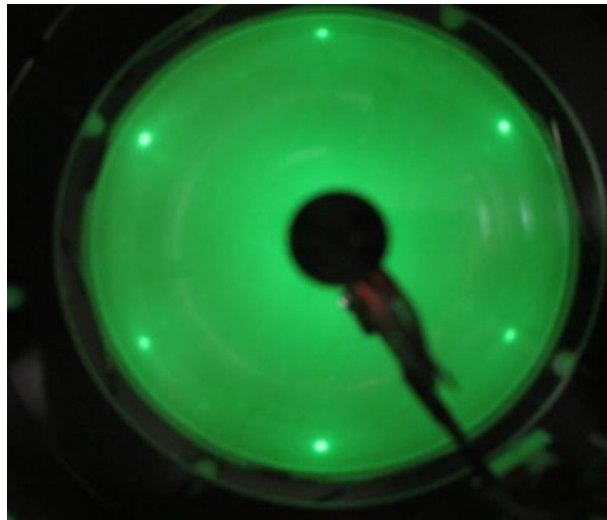


Fig. 17 LEED of graphene over Ni(111)

Various EELS spectra were taken at different angles and plasmon was observed. The spectrum in fig. 11, taken with a primary energy of 100 eV and incident and analysis angles of  $45^\circ$  and  $39^\circ$  respectively, shows the presence of the  $\pi$ -plasmon centered at about 7 eV.. In the same figure, is also presented the spectrum obtained by subtracting from the above spectrum, that obtained in the same geometry on the clean Ni surface. In the subtracted spectrum, where the Ni contribution has been eliminated, the plasmon peak is even more evident.

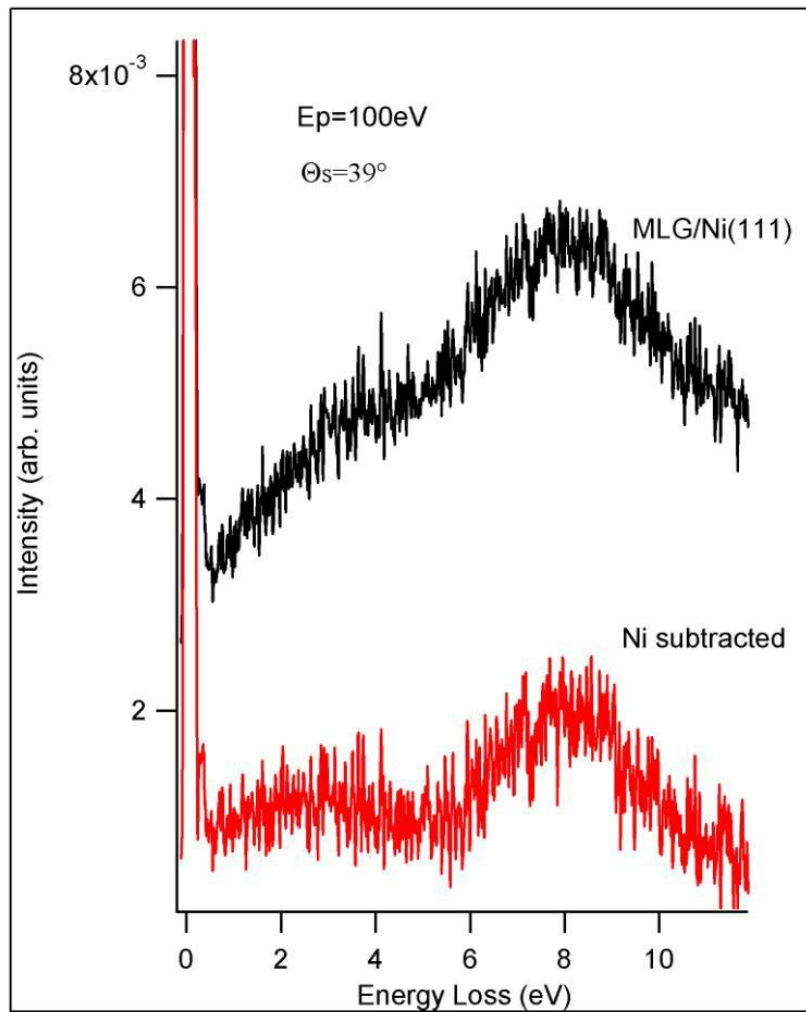


Fig. 18 EELS spectrum of Graphene on Ni(111) (incidence  $45^\circ$ , analyzer  $39^\circ$ ), the red spectrum is the above spectrum after the subtraction of Ni(111) clean spectrum.

With the values observed for Plasmons in different angles, a dispersion curve has been created and the form of the curve is a square root that represents the interband transitions of a two-dimensional plasmon.

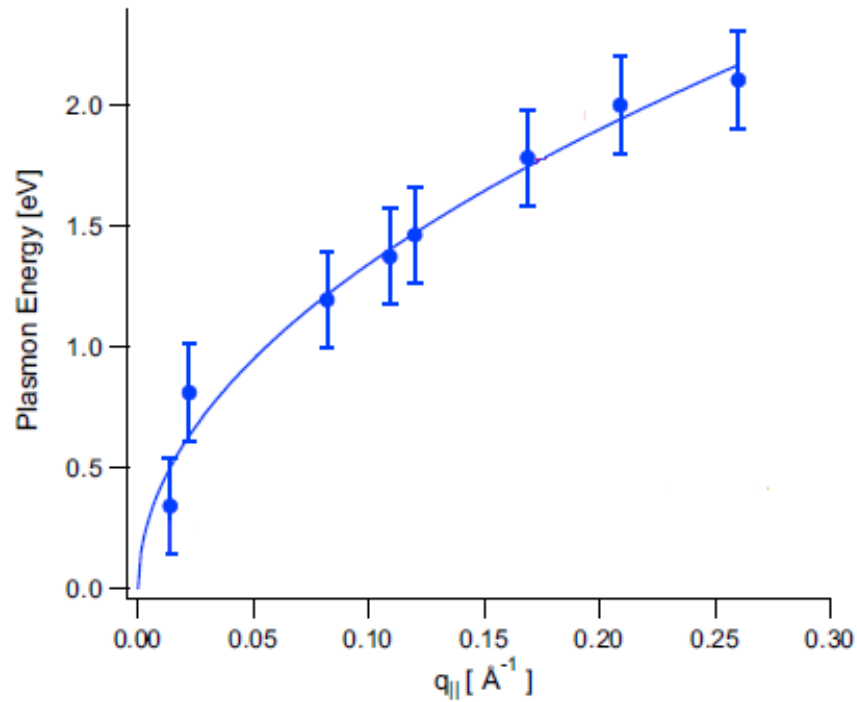


Fig. 19 Graphene on Ni(111) dispersion curve [21]

After this analysis, Cs atoms were dosed onto the graphene-Ni(111) system at room temperature. Cesium is deposited over an out gassed filament that is used for sublimation. Cs coverage was controlled with Auger spectroscopy and LEED, Cs formed a ordinate structure called  $p(2 \times 2)$  with a coverage of 0.25 ML (one monolayer is defined as the number of Cs atoms that equal those of the Ni(111) surface)[21].

After the saturation of the surface with Cs atoms, Auger spectra were collected repeatedly while increasing the temperature in rates of 50 K. In the first Auger spectra is clearly visible the cesium peak and a low contribute of carbon. When the temperature increases cesium peak decreases and the C Auger peak increases. When the carbon intensity is equal to that measured for graphene on Ni(111), the presence of a residual intensity of the Cs peak can be interpreted as due to Cs atoms located in some space between graphene and nickel.

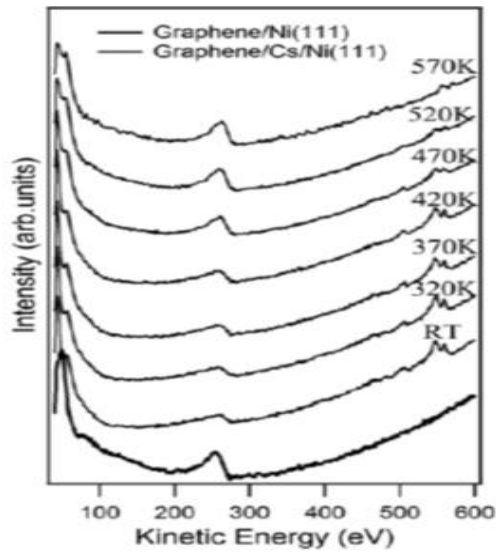


Fig. 20 Cs Auger calibration by using the p(2x2) Cs overlayer on clean Ni(111)[59]

In literature Eberlein et al [22], reported the values of the collective excitations for different layers of graphene obtained by Scanning transmission electron microscopy (STEM).  $\pi$ -plasmon is observed at 4.7 eV in the single layer.

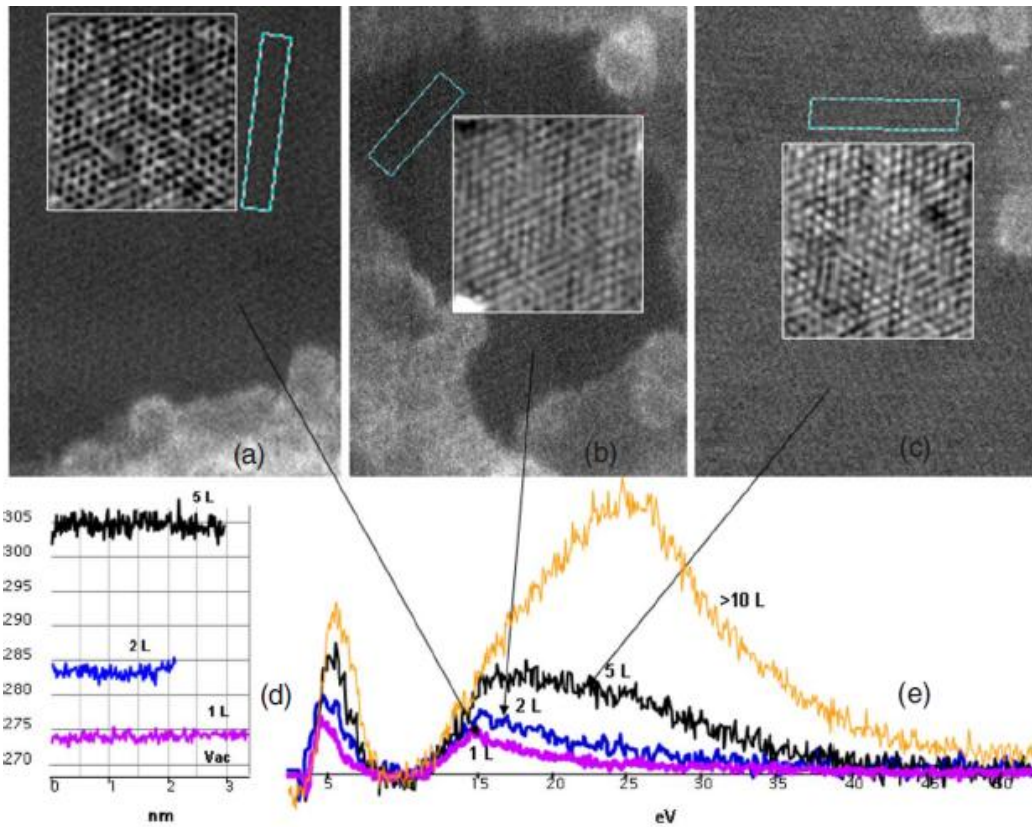


Fig. 21 Scanning transmission electron microscopy(STEM) images of Plasmon contribution of Graphene different layers[22]

The EELS spectra of the system Cesium-graphene-Ni(111) reveals the  $\pi$ -Plasmon peak at 7eV [21] , Fig. 16 shows the curve, which has a quasi-linear behavior, similar to the free-standing graphene dispersion curve reported by M.K Kinyanjui *et al* [23].

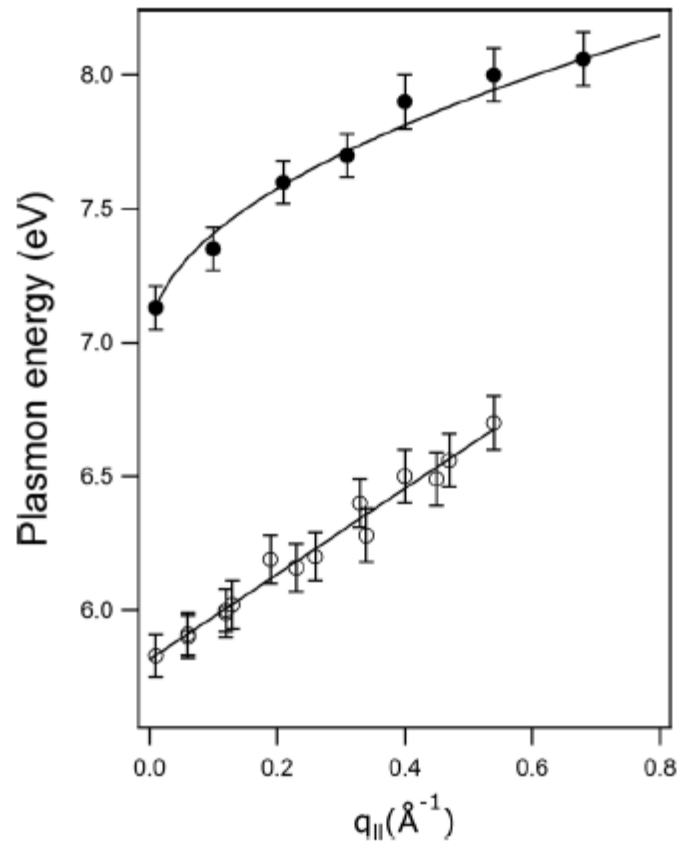


Fig. 22 Energy loss values of the interface- p-plasmon peak plotted vs  $q$  for the Graphene/Ni(111) filled circle and for the Graphene/Cs/Ni(111) system (open circle)[21]

The results are then indicative of an almost perfect isolation of the graphene layer by the intercalated Cs atoms, even if some degree of hybridization is still present, giving the p-plasmon at an energy higher with respect to that observed on free-standing graphene (7 eV vs. 4.7 eV)

## ***2. Graphene from graphite: Exfoliation and oxidation***

## ***2.1 Introduction***

One of the forms to preparing and obtain graphene is mixing graphite with some elements and compounds that can lead ( depending on the preparation ) to graphene with different degrees of defects and the improvement of the characteristic that can be used in several applications.

This approach for obtaining graphene, is known as a top-down approach. This approach has several routes to obtain graphene, but in a general view, this routes can be separated with the general titles of exfoliation and oxidation.

The first stages of those processes produces novel materials with features and functionalities lightly different to those of graphene, and can be used in applications where the graphene does not work at its finest, and for its low production cost are attractive to the scientific community , this materials , are named as “ graphene based materials”.

In this chapter, innovative approaches based in process of exfoliation and oxidation for graphene production are proposed and explored.

## ***2.2 How to obtain graphene (second part)***

As mentioned in the first chapter, there are several methods to obtain graphene. In the top-down approach, graphite is used as the starting material to obtain graphene layers, exfoliation and oxidation processes are the general methods in this approach.

### ***2.2.1 Exfoliation***

Exfoliation is the removal of the outermost layer of a solid in sheets or flakes. Exist numerous exfoliation methods, but, as a general line can be mentioned two procedures: mechanical and chemical exfoliation.

#### ***2.2.1.1 Mechanical Exfoliation:***

Refers to the process where a mechanical force is used to separate graphene layers from graphite[1]. Is the most popular route to obtain graphene due to low cost and easy production. The disadvantage of this technique is that it cannot be used in many applications because the resulting material often contains agent remnants. Nevertheless, this method is still attractive as a facile method to obtain graphene due to its simplicity and the possibility of obtaining graphene with high quality[1], [24]. The more known exfoliation technique is micromechanical exfoliation for its historical value.

Early attempts to micromechanically exfoliate graphene are from 1997, when Ohashi and his group mechanically exfoliated between 20-100 layers of graphene[1].

Several groups worked in this way using AFM tip manipulation but it was in 2004, when started the boom of graphene when Geim and Novoselov exfoliated graphene using scotch-tape: they separate and characterize few and single layer graphene[25].

### ***2.2.1.2 Exfoliation in the presence of solvents***

The bulk graphite can be separate in layers using solution based chemistry. In this process, a polar solvent is used to break the strong Van der Waals forces that stick graphene layers and should prevent their restacking.

Many of the early successes in this kind of exfoliation came for previous works in carbon nanotubes. In 2008, Geim and Novoselov, observing the limitations of mechanically exfoliated graphene, reported a simple method in which graphite was sonicated with dimethylformamide (DMF) to produce thin graphite pieces and some monolayer sheets. Few month later, Hernandez et al[26], made the first systematic about monolayer suspensions of graphene formed with organic solvents as N-methyl-pyrrolidone (NMP)[26], N-Dimethylacetamide(DMA)[26],  $\gamma$ -butyrolactone(GBL) [26] and others.

## ***2.2.2 Chemical preparation***

The chemical preparation of graphene using a chemical treatment consists of two separated reactions: oxidation and reduction. The oxidation reaction is performed using very strong reaction parameters and media so that chemical-physics and morphological characteristics of obtained products are non-homogeneous and difficult to control. Generally, this reaction produces variously sized graphite oxide and graphene oxide materials.

On the contrary, the reduction reaction is a simple, high-yield, easy controlled reaction. For this reason, in this research work the first type of reaction has been stressed in order to realize innovations in reported preparation methods.

### ***2.2.2.1 Preparation of Graphite Oxide by oxidation***

Graphite oxide is the bulk of graphene oxide and is similar to graphite but has a larger layer spacing depending on the preparation procedure. The product has a C:O atomic ratio of 2.0 to 2.9. Is a hydrophilic material and can be easily exfoliated.

The chemical composition of the graphite oxide has been estimated to be approximately  $C_4O(OH)$ [27].

The history of graphite oxide is the same history of graphene oxide and is really extended because started with the first studies of graphite.

Graphite oxide was prepared for the first time by B. C. Brodie in 1859 by a treatment of a mixture of potassium chlorate ( $KClO_3$ ) and fuming nitric acid with graphite with the resulting increase in the overall mass of the flake graphite and a molecular net formula  $C_{2.19}H_{0.80}O_{1.00}$  [28].

Approximately 40 years after, L. Staudenmaier improved Brodie's method by adding sulfuric acid to the mix and adding the chlorate in multiples phases of the reaction[28].

Hummer's method uses the graphite prepared with a mixture of a concentrated sulfuric acid ( $H_2SO_4$ ), sodium nitrate ( $NaNO_3$ ) and potassium permanganate ( $KMnO_4$ )[29] making an improvement in the quality of the oxide graphite, the preparation time (about two hours) and eliminates the formation of acid fog.

The Hummer's method has the disadvantages of releasing toxic gases and the difficulty to remove the residual  $N_2O_4$  and  $NO_2$ [30].

Looking for a less aggressive treatment, Marcano et al [31] in 2010 proposed a modification of the Hummer's method excluding  $NaNO_3$  and adding a mixture of  $H_2SO_4/H_3PO_4$  and increasing the quantity of  $KMnO_4$ ; this changes resulted in an increase in the security of the process because the production of toxic gases is reduced, and there are no large exothermic reactions. The final product is more oxidized, has more regular structure and makes less damage to the basal planes of graphite than the Hummer's method.

### ***2.2.2.2 Graphene oxide***

GO is a hydrophilic material[32]–[36] that can form stable suspensions in aqueous media. This hydrophilic nature, combined with the high surface area and functional group density, allows for a wide variety of chemical functionalization to be performed on GO sheets. GO is considered as a building block for novel graphene based-nanomaterials[6][37].

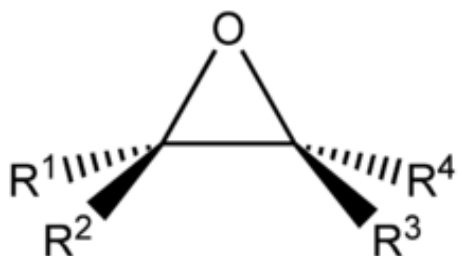
GO does not exist as a static structure with a definite set of functional groups. The Ajayan model is held by the fact that GO prepared by chemical oxidation exhibits strong variance in its structure and degree of oxidation depending on the particular oxidants used, but also on the graphite source and reaction conditions[37].

To obtain graphene oxide, graphite oxide must be exfoliated by sonication or prolonged stirring in water. Graphene oxide disperses well in water due to negative surface charges on the sheets that arise from the carboxylic acid groups and keep it from reaggregating[1].

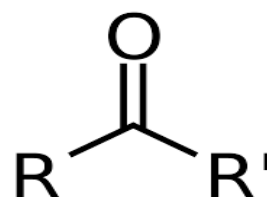
### 2.2.2.3 GO structure:

In graphene oxide the common functional groups are[38]:

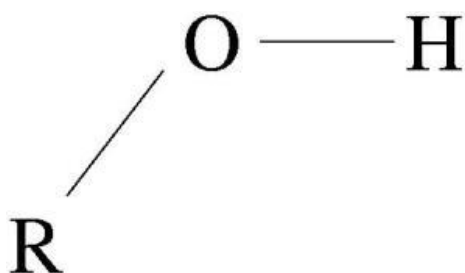
a) Epoxy groups (C-O-C)



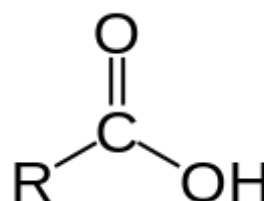
b) Carbonyl groups



c) Hydroxyl groups (OH)



d) Carboxyl groups (-COOH)



The GO structure depends on the oxidation conditions, and the graphite precursor. For that reason, Dreyer et al consider that GO may be thought of as a family of materials[39] that can have differences between them. In the fig. existing models for the GO structure are proposed. There are just little modifications between them.

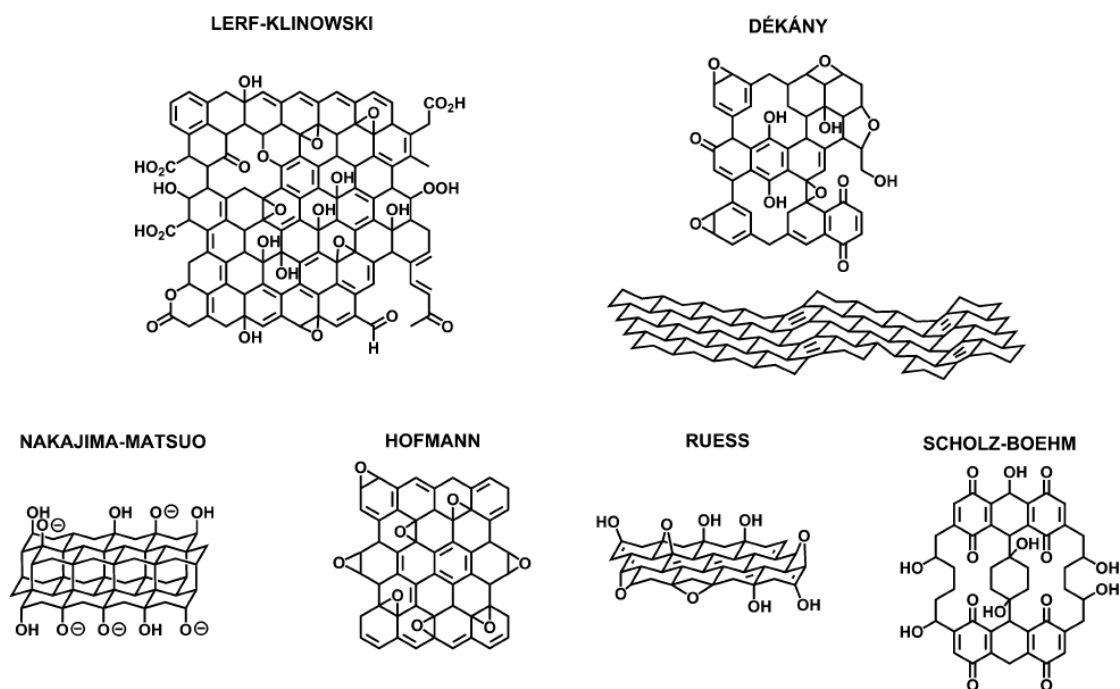


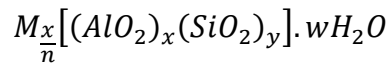
Fig. 23 Proposed atomic models for Graphene oxide[39]

Hofmann in 1939 proposed a simple models with epoxy groups distributed randomly over the basal plane[28] Ruess suggested a structure with epoxy and hydroxyl and ether groups that forms oxygen brigdes between carbon atoms. Scholz and Boehm in 1969 presented a structure with carbonil and hydroxyl groups[28]. Nakjima-Matsuo proposted (1994), as difference from other models that oxygen atoms of epoxy groups had adyacent layers[28].

The Lerf-Klinowsky model is the most widely accepted, this model takes elements from Sholz-Boehm’s and Ruess’, it considers that hydroxyl and epoxide groups “decorate” the basal plane which are segregated into island[39] [28] and depending on the pH of the solution, the carboxyl groups are present on the edges of the sheets.

## 2.3 Zeolites

Zeolites are crystalline aluminosilicate made of elements from groups IA and IIA in the periodic table. Chemically they are presented by the general formula:



where  $n$  is the valence of cation  $M$ ,  $w$  is the number of water molecules per unit cell,  $x$  and  $y$  are the total number of tetrahedra per unit cell (values in the range 1-5). Zeolites consist of interconnected  $SiO_2$  and  $AlO_2$  tetrahedra and cations<sup>+</sup> (see fig.18). Actually exist 170 different types and about 17 of them have commercial interest.

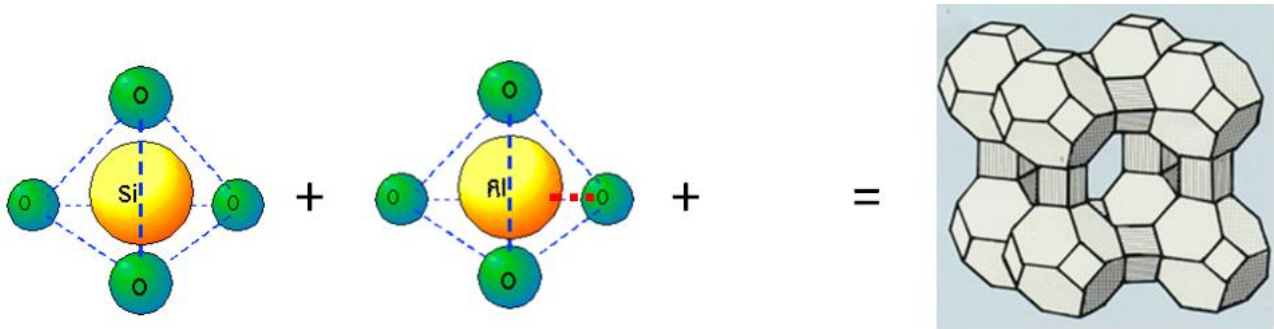


Fig. 24  $SiO_2$  and  $AlO_2$  tetrahedra that forms zeolite.

Zeolites can be divided into natural and synthetic. Natural zeolites are minerals of volcanic origin and typically occur in cavities in basaltic and volcanic rocks. They can be found in sedimentary deposits and some occur in large monomineralic deposits suitable for mining. Zeolites can be used in adsorbent applications, concrete, paper, soil conditioner and fertilizers.[40].

The word zeolite derived from the greek words, “ζεο” and “λιθος” meaning “to boil” and “ a stone” [40].

In 1756, A. F. Cronsted discovered the first mineral zeolite. He analyzed some properties and classified them as a group inside the minerals.

21 years after, Fontana observed an adsorption phenomenon in the presence of charcoal, several groups observed in the next years that zeolite crystals could reversibly be dehydrated with

no apparent change in their morphology. reference In 1925, Weigel and Steinhoff reported the first molecular sieve effect[40].

The pioneering work about the zeolite synthesis and adsorption was made between mid-1930's to 1945 by R. M. Barrer which presented the first zeolite classification[41]. depending on the dimension of the molecules and the velocity of adsorption at room temperature.

After this work, zeolites started to grow commercial interest because Barred showed a synthetic analog of a type mineral zeolite called Mordenite. [41]

Between 1949 and 1954, R.M. Milton and D. W. Breck from Union Carbide developed commercial synthetic zeolites type A, X, and Y[40].

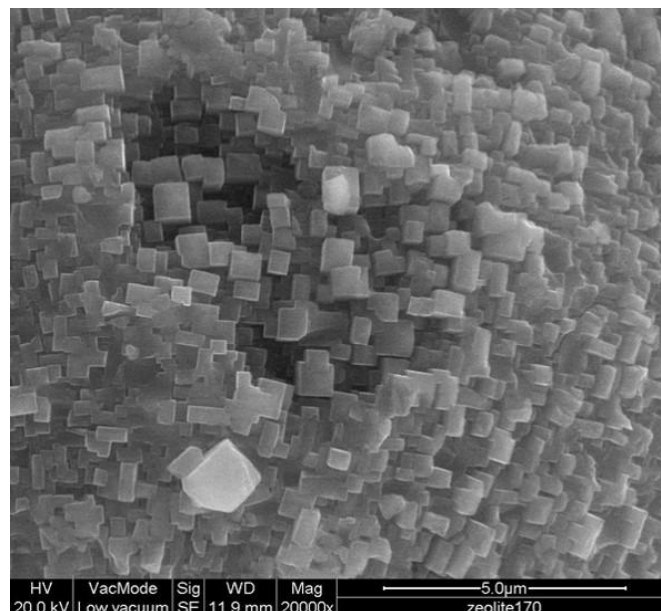


Fig. 25 Image of zeolite type A took with a Scanning electron microscope (SEM)

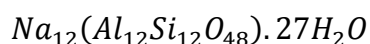
Zeolite A was the first synthetic zeolite commercialized as an adsorbent material for separation and purification. Union Carbide started its commercialization in 1953.

Henkel in 1974 introduced zeolite A in detergents as a replacement for the environmentally suspect phosphates. Union Carbide inserted in 1977 zeolites for ion-exchange separations.

Zeolites have interesting properties as mentioned indirectly earlier in this section. Between them, should be remarked the following:

- **Uniform pore dimensions**
- **Chemical stability**
- **The capacity of modification:** Zeolites are ideal for modifications because the metal-oxygen tetrahedrals are in contact with the internal zeolite surface, and this allows for modifications such as exchange of charge-compensating cations [40], replacement of atoms Si or Al in the framework and the introduction of metal particles.
- **Has the ability to develop internal acidity,** which makes zeolites materials suitable to catalyze organic reactions.
- **High thermal stability**
  
- **High specific-surface-area (400 m<sup>2</sup>/gr)**

The zeolite used in this thesis is the type A that has formula:



Has 11.4 Å cavities, has a Si/Al =1 (the quantity of Si and Al are the same), and is actually used in detergents, and hard water treatment.

## ***2.4 Experimental techniques***

### ***2.4.1 Scanning electron microscopy (SEM)***

The SEM microscope was invented in 1931 by E. Ruska and M. Knoll for observation of the surface of organic and inorganic materials. reference

In the SEM mechanism, an electron gun controlled by a series of lenses generates an high energy beam in the range of 2-10 nm in width and in the range of energy from 1 to 40 keV. The scanning electron beam is produced in an electron microscope column[42] that has a field

emission cathode. The microscope performs under vacuum to reduce the mean free path of electrons.

The electrons scattered from the surface of the sample produce a variety of signals, between them, the backscattered and the secondary signals are usually converted in an image of the surface. The samples must be electrically conducting to avoid the accumulation of charge that can result in false images. In the case of non-conducting samples, they are covered with a conducting layer (normally gold, carbon or platinum ) which makes the surfaces conductive.

SEM normally includes other detectors: Energy dispersive X-ray analysis (EDX) used for chemical analysis and Electron back scatter diffraction (EBSD) used to examine the crystallographic orientation of the substrate.

The samples in this work were characterized using a microscope model Quanta FEG400F7 (FEI) with resolution up to 10 nm.



Fig. 26 Scanning Electron Microscope- FEI Quanta 200 Instrument

SEM is normally used in graphene research to determine domain morphology, nucleation density, domain size, growth rates and sample coverage. As a disadvantage, this technique does not allow the determination of the exact number of the layers.

## 2.4.2 Transmission electron microscopy (TEM)

Transmission electron microscopy (TEM) is a kind of microscopy very similar to SEM, is used for the study of samples from micron scale down to atomic resolution[1] .

An electron beam, emitted by an electron gun by thermionic or field emission under UHV conditions, is injected into the microscope column by an accelerating voltages (in the range of 200-300 kV) focused accurately by electromagnetic condenser lenses and passes through a very thin specimen (less than 50nm thick) onto fluorescent screen forming a visual image. As the electrons pass the sample, they are scattered by the electrostatic potentials of its atoms.

TEM frequently include other chemical analysis tools, such as detectors for energy-dispersive X-ray analysis (EDX) and electron energy loss spectroscopy (EELS).

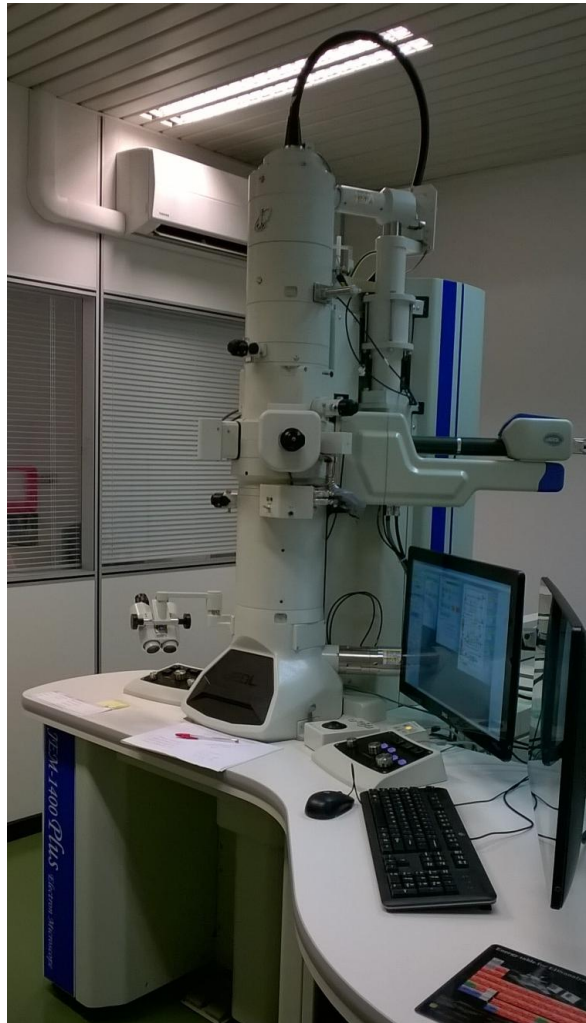


Fig. 27 Transmisison Electron Microscopy

The Transmission Electron Microscopy (TEM) images were obtained in a microscope model TEM-1400 plus Electron Microscope.

### ***2.4.3 Raman spectroscopy***

Raman spectroscopy is based on the Raman effect. Light from a laser incides on a substance and the scattered light is analyzed spectroscopically. The Raman spectroscopy is used as a means of determining molecular structure and as a tool in chemical analysis.

This technique provides chemical and structural information of almost any organic and inorganic composite material. Also is widely used to characterize carbon systems because gives information about the presence of defects and disorder.

This spectroscopy technique is based in the inelastic scattering of light called as Raman effect, in honour to C.V. Raman that received the Nobel prize of Physics in 1930 for his work.

The most usual scattering phenomenon that can result from Raman scattering involves phonons. In the Raman process, an incident photon with energy

$$E_i = E_{laser}$$

and momentum

$$k_i = k_{laser}$$

reaches the sample and is scattered, resulting in a photon with a different energy and momentum,  $E_s$  and  $k_s$  respectively. For the energy and momentum conservation:

$$E_s = E_i \pm E_q$$

$$k_s = k_i \pm q$$

Where  $E_q$  and  $q$  are the energy and the momentum of the phonon that is created or annihilated in the Raman event[43].

The basic concepts of this spectroscopy can be introduced within the framework of classical electromagnetism[43].

The polarization of a crystal (or a molecule) may be approximated by summing the product of the polarizability of the individual atoms in the crystal (or molecule) times the local electric fields.

$$P = \sum_j N_j p_j = \sum_j N_j \alpha_j E_{local}(j)$$

Where

$N_j$  is the atomic concentration of each species.

$p_j$  atomic polarization.

$\alpha_j$  polarizability of an atom in a material.

$E_{local}$  is the local field given.

If we consider  $E_{local} = E + \left(\frac{4\pi}{3}\right)P$  and solving for susceptibility  $\chi$  we obtain:

$$\chi = \frac{P}{E} = \frac{\sum_j N_j \alpha_j}{1 - \frac{4\pi}{3} \sum_j N_j \alpha_j}$$

Light scattering can then be understood simply on the basis of classical electromagnetic theory.

When an electric field is applied to a solid, the polarization results as:

$$P = \vec{\alpha} \cdot E$$

Where  $\vec{\alpha}$  is the polarizability tensor of the atom in the solid. With this result a classical description of the Raman effect can be obtained.

The electric field of the light in a scattering experiment oscillating at an optical frequency  $w_i$  can be expressed as:

$$E = E_0 \sin w_i t$$

The lattice vibrations in the solid modulate the polarizability  $\alpha_0$  of the atoms, where:

$$\alpha = \alpha_0 + \alpha_1 \sin w_q t$$

And  $w_q$  is a normal mode frequency of the solid that couples to the optical field so that the polarization which is induced by the applied electric field becomes:

$$P = E_0 \left[ \alpha_0 \sin(w_i t) + \frac{1}{2} \alpha_1 \sin(w_i - w_q) t - \frac{1}{2} \alpha_1 \sin(w_i + w_q) t \right]$$

Light will be scattered both elastically and also inelastically, when is scattered elastically at a frequency  $w_i$  is named Rayleigh scattering; when is scattered inelastically two situations can happen: if the light is downshifted by the natural vibration frequency of the atom this process for the emission of a phonon is known as Stokes process, in the case that the light is upshifted by the same frequency is named as the anti-Stokes process for the absorption of a phonon

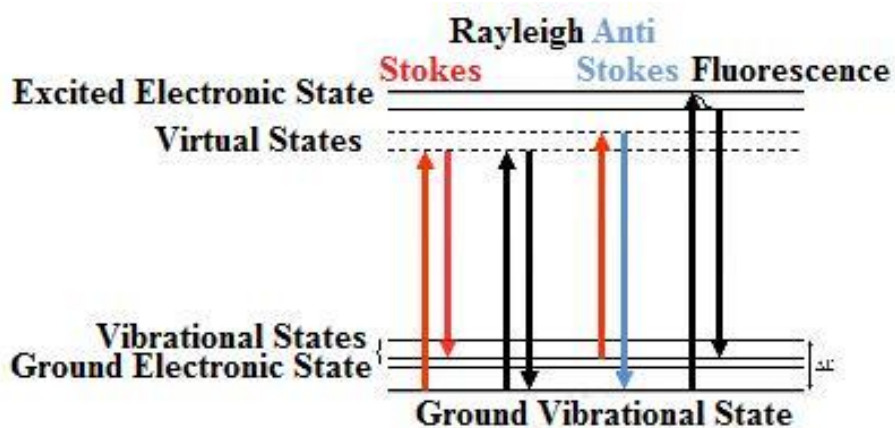


Fig. 28 Jablonsky Diagram used for represent Raman and Raleigh scattering:

In our experiments a Thermo Fisher DXR Raman microscope with a 532 nm line was used.



Fig. 29 Thermo Fisher DXR Raman microscope

The Raman spectrum of Graphene is unique and evolves with the number of layers. The graphite spectrum is characterized by the presence of two strong peaks at  $1580\text{ cm}^{-1}$  named G band and  $2700\text{ cm}^{-1}$  named G' band.

In the Raman spectra of graphene (in presence of defects), other peaks are observed. The peak with highest intensity near at  $1350\text{ cm}^{-1}$  is named as D band, is only observed in the presence of defects (is proportional to the amount of disorder of the sample or at the edge of the sample) and is associated to a breathing-like motion of carbon atoms in the hexagon that becomes Raman active due to the loss of lattice symmetry.

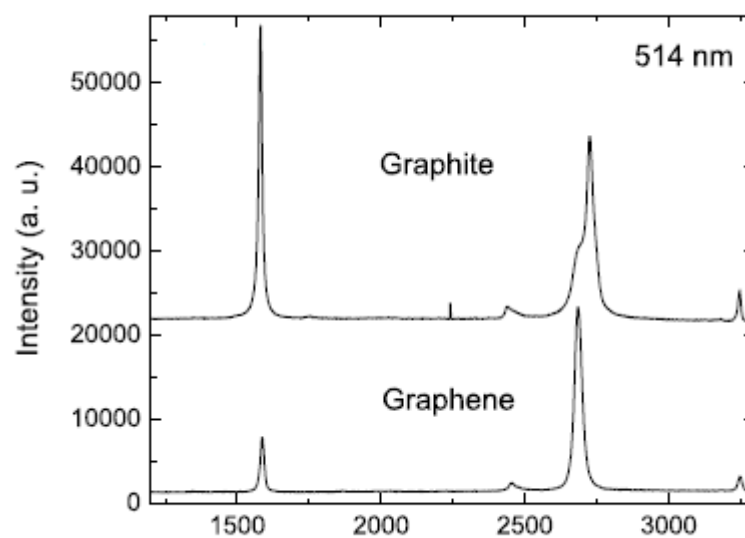


Fig. 30 The typical Raman spectrum of bulk graphite and graphene with an incident laser, taken from Ferrari et al, 2006 [5]

The ratio between the intensities of the disorder induced D band and the first order graphite G band,  $\frac{I_D}{I_G}$  provides a parameter that can be used for quantifying the amount of disorder.

Disorder Raman spectra has its origins on the phonons in the interior of the Brillouin zone ( $q \neq 0$ ) that contributes in the spectra as a higher order Raman process[38].

## 2.5 Results

As mentioned in the introduction of this chapter, when making graphene, in the first stages of the process can be obtained the so call “graphene-based nanomaterials ” that depending on the preparation have some features lightly different to those of graphene.

With the scope to obtain graphene, some graphene- based nanomaterials were prepared by the process of simultaneous exfoliation/oxidation. This experiments were made using a sonication bath. After that, a very well known method to prepare graphene oxide was improved by adding a mesoporous material.

### 2.5.1 Graphite And Hydrogen Peroxide( $H_2O_2$ ):

At a room temperature, 200 mg of graphite was sonicated for 3 hours with 12 ml of hydrogen peroxide ( $H_2O_2$ ) 30%( $v/v$ ) (Fluka chemika- Sigma Aldrich), without presenting visible changes. SEM image of graphite showed a separation of some layers, but not in a quantity that can be considered as interesting. In Raman spectrum peaks at 1347  $cm^{-1}$ , 1579  $cm^{-1}$  and 2717  $cm^{-1}$  can be observed and, the last two peaks are near approximately at the values of the graphite peaks in Raman spectrum in literature and the commercial graphite used for this experiments(See: table 1, Fig. 31).

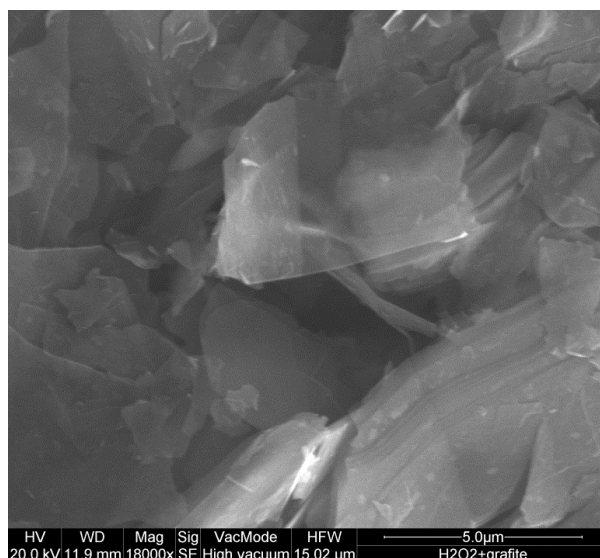


Fig. 31. SEM image of graphite and hydrogen peroxide

## Graphite and hydrogen peroxide

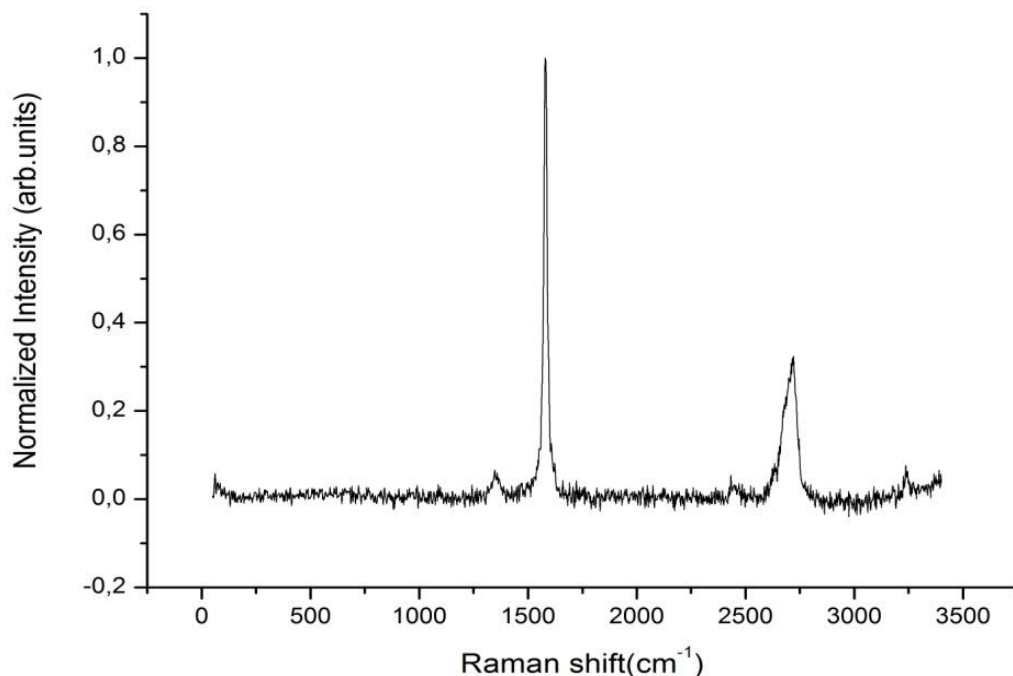


Fig. 32 Raman spectrum of graphite with hydrogen peroxide

### ***2.5.2 Graphite With Hydrochloric Acid (HCl) And Graphite With Nitric Acid (HNO<sub>3</sub>):***

In order to observe the behavior of graphite when exposed to acids, 2 ml of hydrochloric acid (Sigma – Aldrich) was sonicated at 30 ° C for 30 minutes with 53.4 mg of graphite without presenting visible changes, solid sample was washed in 800 ml of distilled water and after was dried at room temperature over a stainless steel surface.

Graphite was mixed with 2 ml of nitric acid 65%(v/v) with sonication at room temperature for 30 minutes without visible changes. The sample was washed in 800 ml of distilled water and after was dried at RT over a stainless steel surface.

In SEM images, both show the formation of a surface that made impossible to see the graphite layers.

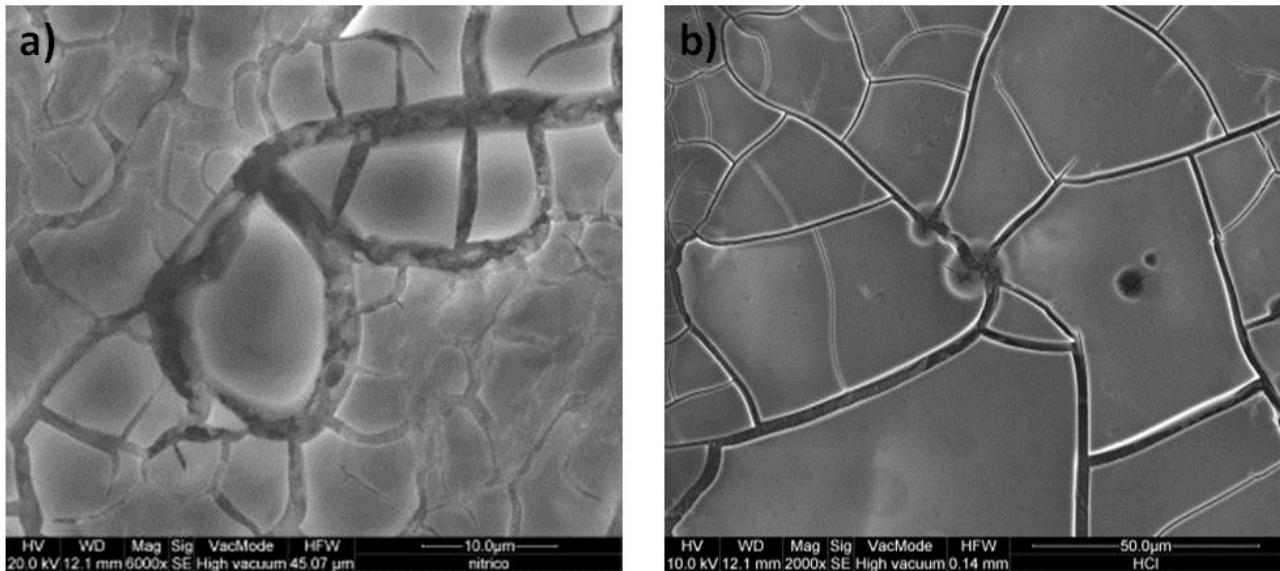


Fig. 33 SEM images of a) graphite with nitric acid and b) graphite with hydrochloridric acid.

As SEM did not revealed the presence of graphite layers (probably for the interaction with air). Raman spectra were obtained for both samples and compared with the graphite used for the experiments.

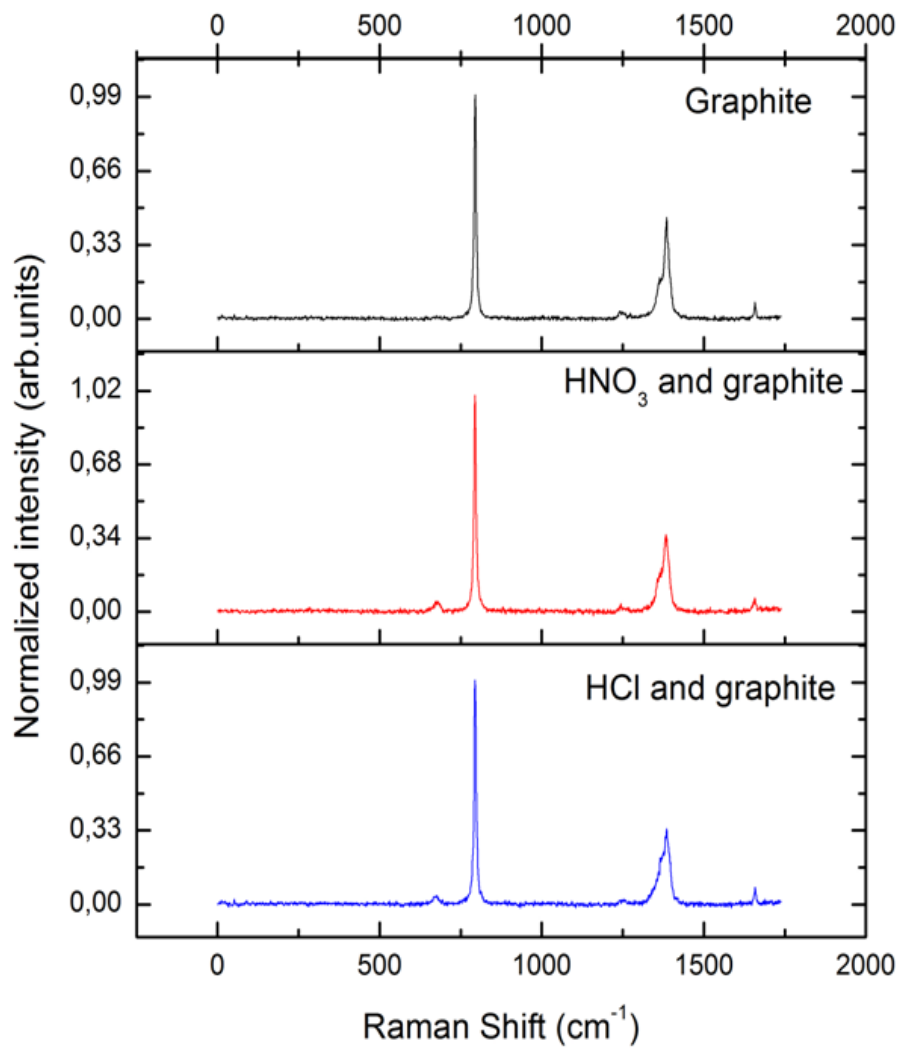


Fig. 34 Raman spectra of Graphite and graphite with some acids.

The compared spectrums confirmed that there is not big changes in structure, just a little introduction of defects(see table1 for peak values).

### 2.5.3 Graphite Oxide (*Graphite and Aqua Regia*)

As mentioned in previously in this work, graphite can be attacked chemically by some acids and combinations of them, between these combinations can be called 'Aqua regia' that is a combination of hydrochloric acid and nitric acid. In the literature, Kim *et al* [11] and Ambrosi *et al*[44]used aqua regia for cleaning GO to obtain graphene.

3 ml of hydrochloric acid 37% (*v/v*) and 9 ml nitric acid 65% (*v/v*) and 200 mg graphite reacted spontaneously without increasing the temperature and acquired a yellow color. This mixture was sonicated for 15 min and the formation of foam and the change to a color dark yellow was observed.

When the materials finished the spontaneous reaction after the sonication, the solid product observed was distributed in the beaker used for the experiment in 3 parts as shown in the scheme (fig. 35). The three samples were named as "sotto acqua regia" (bottom sample), "centro acqua regia" and "sopra acqua regia" (top sample), a little repetitive, but easy for remembering the procedence of the sample. The samples were washed with same procedures used with other cases.

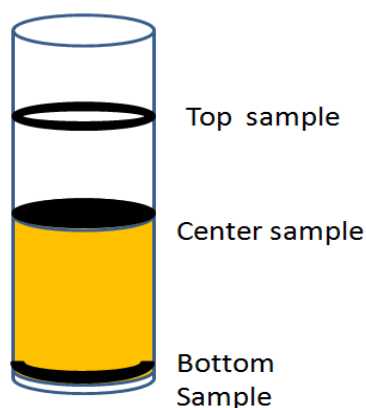


Fig. 35. Distribution of the final product.

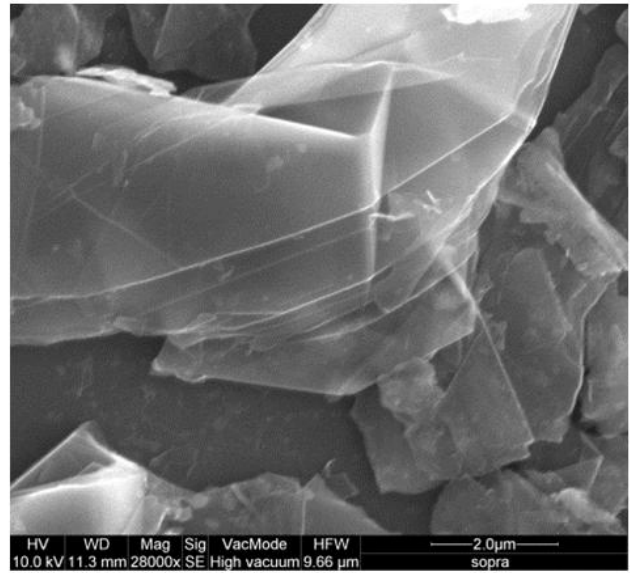
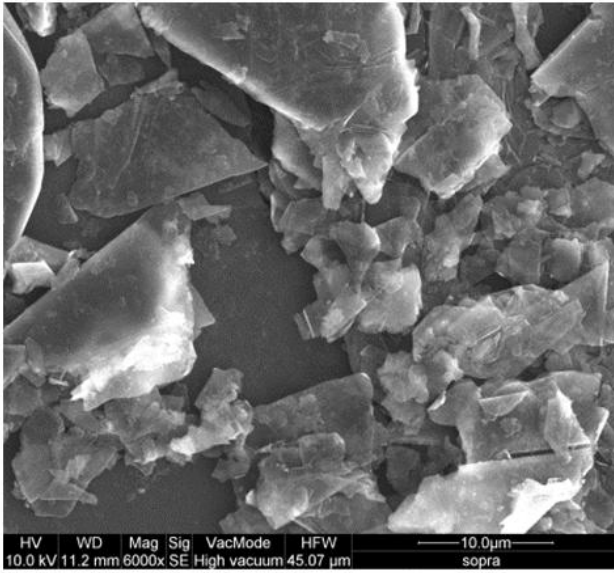


Fig. 36 SEM image of top sample graphite and aqua regia.

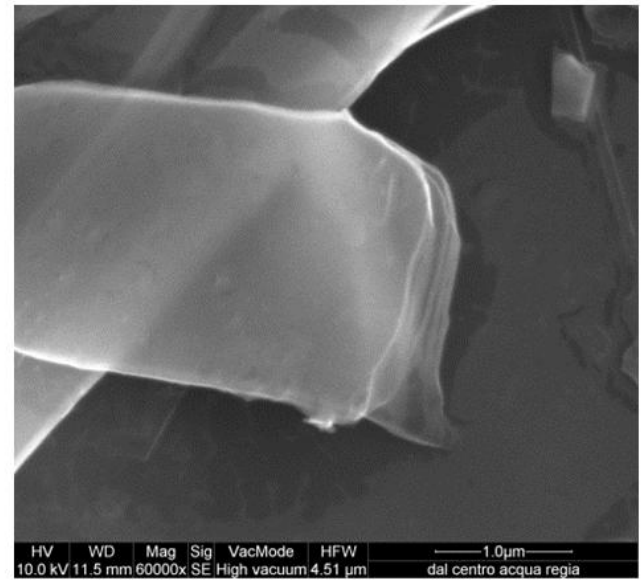
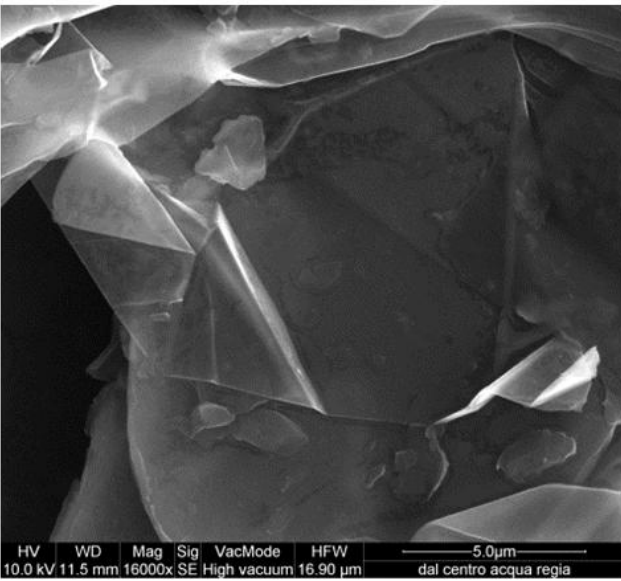


Fig. 37 SEM images of the center part of the sample graphite and aqua regia

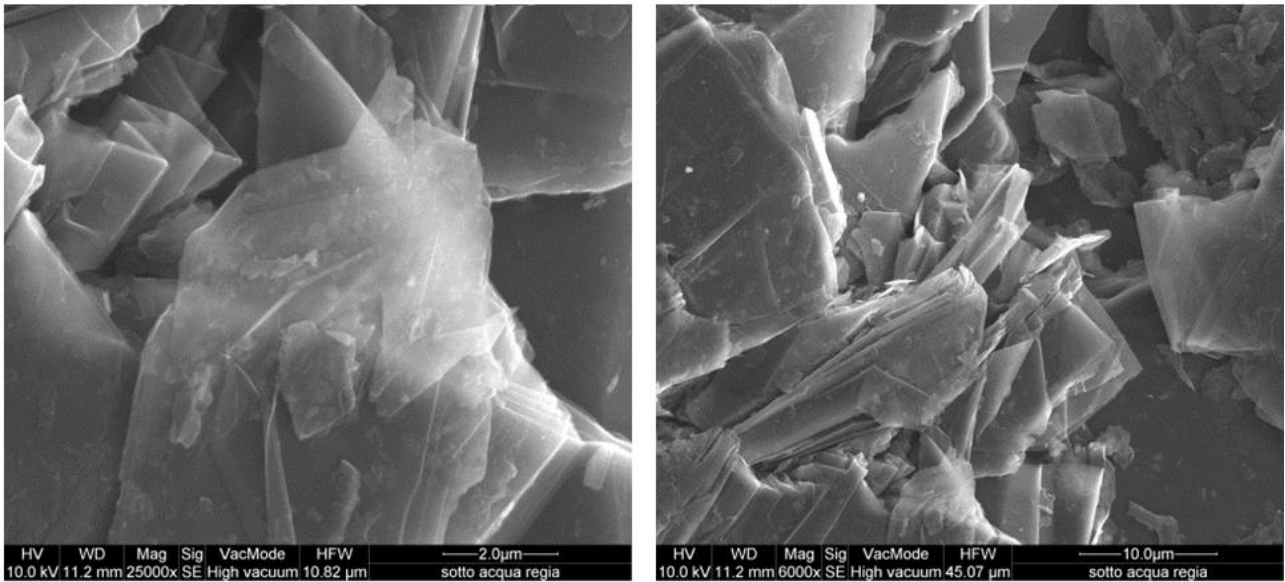


Fig. 38 SEM images from the bottom part of the sample.

In the SEM analysis was observed multiple graphite layers. Even though it looks like in some parts the graphite is transparent, these layers are not thin. TEM images showed similar results, a group of graphite layers can be easily appreciated.

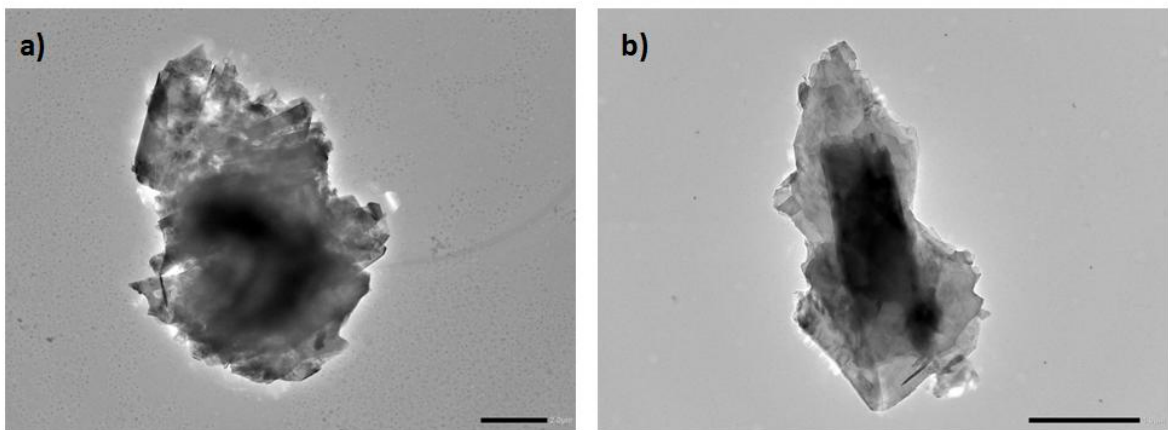


Fig. 39 TEM images of graphite with aqua regia

The Raman spectra of graphite with aqua regia have the same peaks position for the three selected samples. Compared with graphite showed that a little quantity of disorder was introduced in the samples.

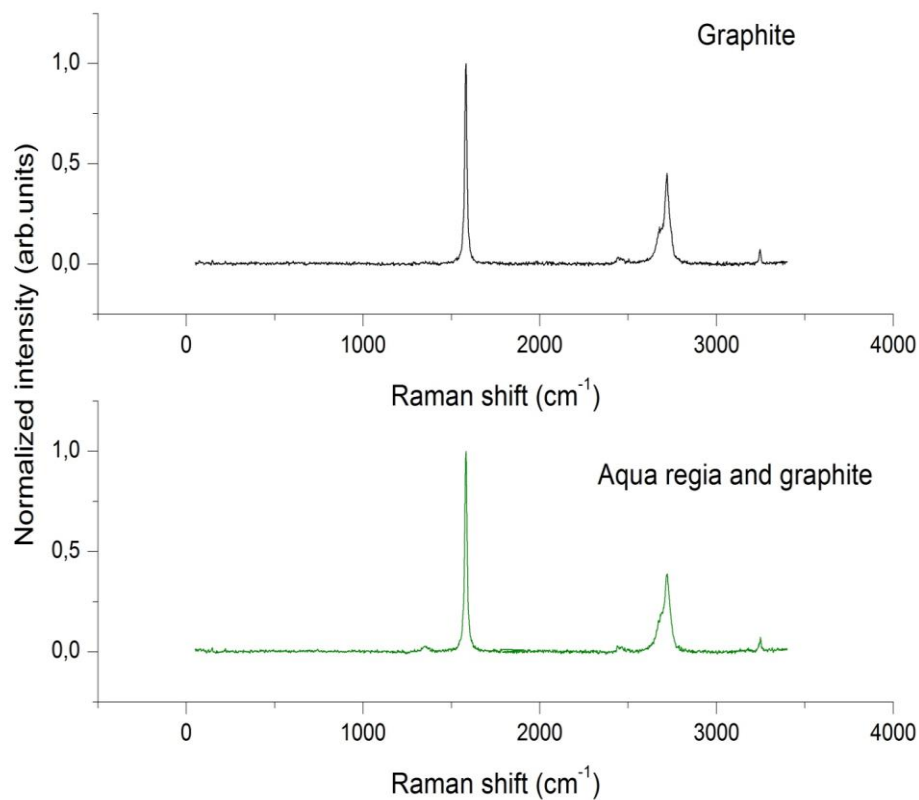


Fig. 40 Raman spectra of graphite and graphite and aqua regia

Changing the combination of the acids that compounds the aqua regia was used, in this case, 4.5 ml of hydrochloric acid at 37% ( $v/v$ ) and 1.5 ml nitric acid at 65%( $v/v$ ) were sonicated for 30 minutes with 50 mg of graphite, without presenting any reaction and changes in the color. Raman spectroscopy showed a little amount of disorder as the first aqua regia combination, data is not showed.

Table 1

	Peak D ( $\text{cm}^{-1}$ )	Peak G ( $\text{cm}^{-1}$ )	Peak G' ( $\text{cm}^{-1}$ )
Graphite (Jorio, 2011)	0	1580	2700
Graphite (reagent)	0	1581	2721
Graphite with $\text{H}_2\text{O}_2$	1347	1579	2717
Graphite with HCl	1348	1581	2719
Graphite with $\text{HNO}_3$	1356	1579	2711
Graphite with aqua regia	1350	1581	2717

## 2.5.4 Oxide Graphene with Zeolite 4A

In this part of the thesis, a very-well known method for prepare graphite has been modified by the introduction of a crystalline aluminosilicate. In pursuance of observing the results of this innovative approach with respect to the Hummer's improved method[31], [45], the reaction has been performed in the presence and in the absence of zeolite crystals to compare the chemical-physics characteristics of the obtained materials.

Natural graphite flakes (Pingdu Huandong Graphite Co., Ltd.) were oxidized using two methods: Hummer's improved method (Marcano *et al*) and Hummer's improved method plus zeolite.

For Hummer's improved method[31], [45], 1 g of natural graphite was added to a solution of  $\text{H}_2\text{SO}_4 / \text{H}_3\text{PO}_4$  with 6 g of  $\text{KMnO}_4$ , the mixture produced an exothermic reaction, and after that it was heated to 50 °C and stirred for 12 hours, and cooled down to room temperature. After, a solution of 133.33 ml of ice with 1ml of  $\text{H}_2\text{O}_2$  ( 30% ( $v/v$ )) was added slowly to the mixture.

The final solution was washed with ethanol and distilled water. The remaining material was sonicated three cycles (45 mins each one) using an ultrasonic processor (UP100H-Hielscher) obtaining a colloidal homogeneous solution that was kept at RT in a vessel for more than 4 months.

In the innovative approach proposed, 1 g of graphite powder and **1 g of zeolite 4A** were placed in a flask with 6 grams of potassium permanganate ( $\text{KMnO}_4$ ). Then, a mixture of 120 ml of  $\text{H}_2\text{SO}_4 / \text{H}_3\text{PO}_4$  was added dropwise (the suspension becomes dark green), while stirring at 100 rpm (magnetic stirrer) at a temperature of 20 ° C.

After 10 minutes, the temperature dropped to 18 ° C and the suspension expelled dark red vapors. An ice bath was used to maintain the temperature at 50 ° C for 12 hours then it was cooled to room temperature.

After this time, hydrogen peroxide ( $\text{H}_2\text{O}_2$ ) at 30% ( $v/v$ ) was added and the suspension showed a light brown color; the remaining solid was washed with 66.66 ml water, 66.66 ml of HCl

30% and 66.66 ml of ethanol and filter with a silicon filter (70 nm ) and this procedure is repeated twice with other filtration processes, and after that washed with water several times. The product maintained a light brown color and was leave in water as a colloidal solution.

For commodity, after this point, GO+ 4A will be the short name used for the Hummer's improved method plus zeolite.

After the first filtration GO+ 4A and GO made by Hummer's improved method were dried at room temperature over a stainless steel surface then the obtained products were characterized. SEM images revealed the strong presence of the zeolite under a transparent sheet.

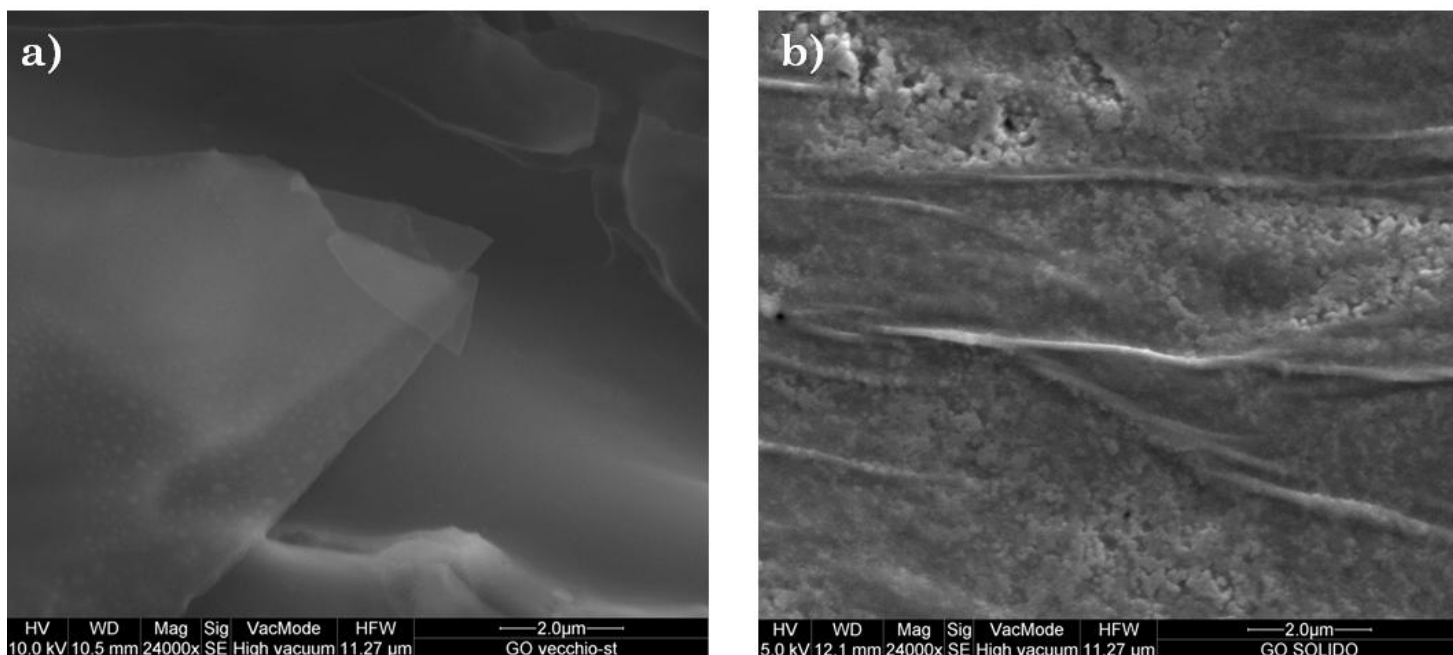


Fig. 41 SEM images of a) GO (Hummer's improved) b) GO+4A after first filtration

Microphotographs obtained before washing the products revealed that very large, homogeneous and transparent, graphene oxide layers were synthesized. So, processes of centrifugation or sonication necessary in the Hummer's improved method of Marcano *et al* (where the reaction product should be centrifuged at 4000 rpm for 4h between the filtration and washing process and sonicated) were avoided. After that, final products were diluted in 800ml of distilled water and dried at RT.

Raman spectra showed D peak at  $1346\text{ cm}^{-1}$  and G peak at  $1589\text{ cm}^{-1}$  with a  $I_D/I_G = 0.85$  for the GO prepared with Hummer's improved method and D peak at  $1354\text{ cm}^{-1}$  and G peak at  $1608$  with a  $I_D/I_G = 0.84$  for the GO with Zeolite 4A, that coincides with the values reported in literature by Chen *et al* (D peak =  $1350\text{ cm}^{-1}$ , G peak =  $1590\text{ cm}^{-1}$ )[46] and Marcano *et al* (D peak  $1350\text{ cm}^{-1}$ , G peak =  $1590\text{ cm}^{-1}$ )[31], the shifted values of GO+4A may be due to zeolite presence but can be concluded that both samples are oxidized.

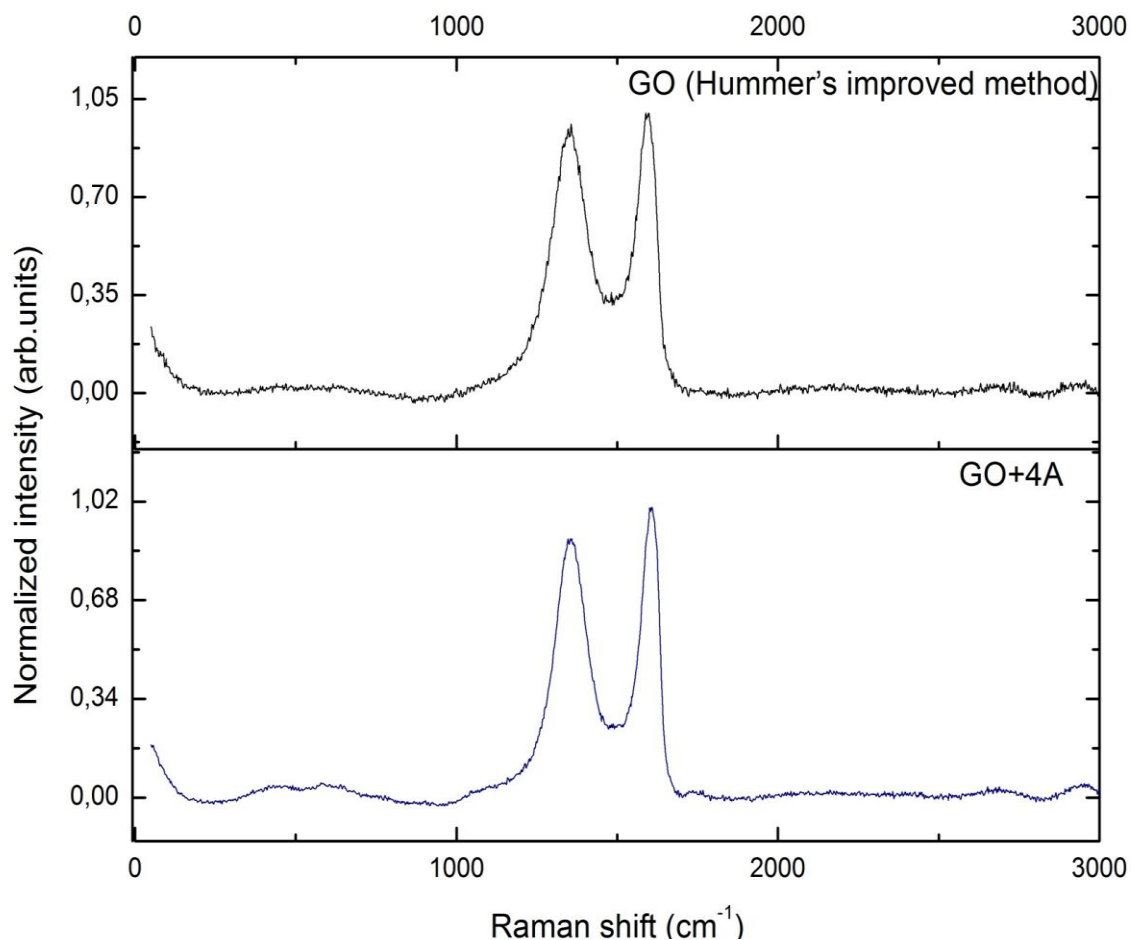


Fig. 42 Raman spectra of GO and GO+4A

For a non-expert observer, the difference between the Hummer's improved method and the innovative modification in Hummer's improved method presented in this work can not be easily distinguished, for that reason new images SEM were taken (See fig. 43).

The flakes were clearly observed, with the notorious characteristic that these flakes were transparent, thin and extended, and corrugations over the zeolites crystals are observed.

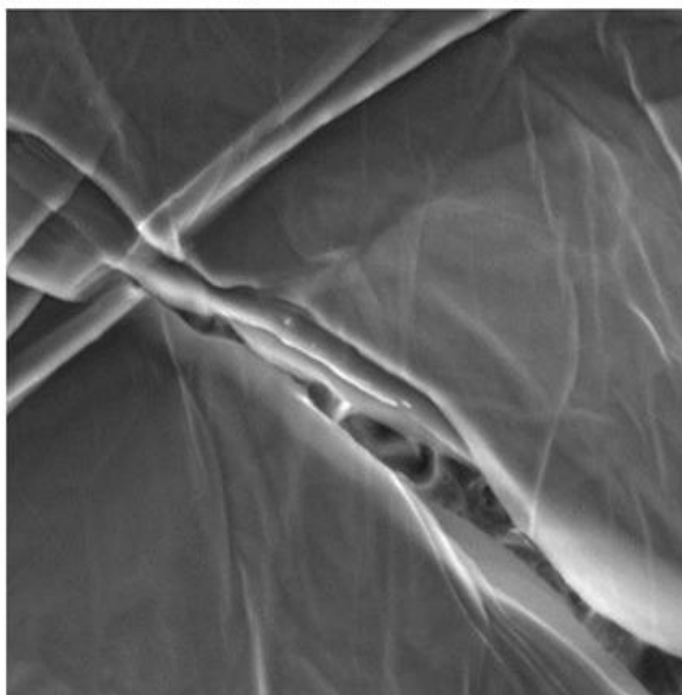
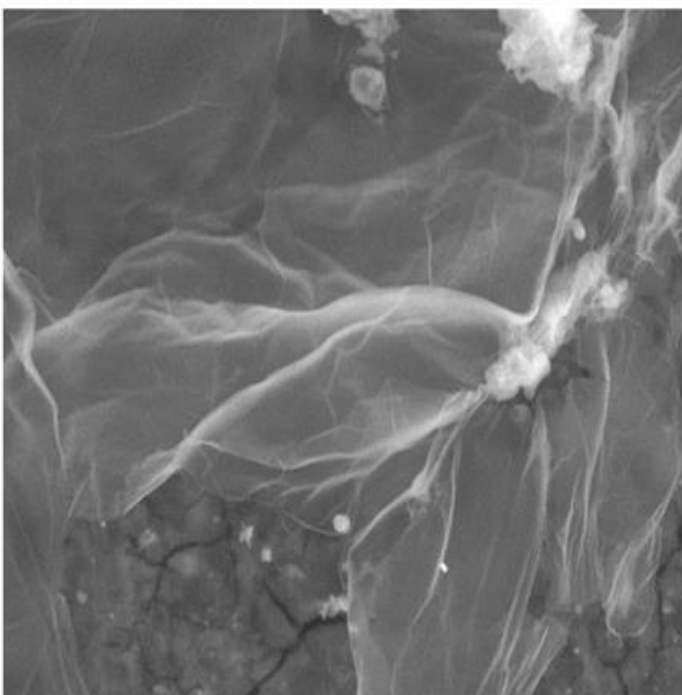
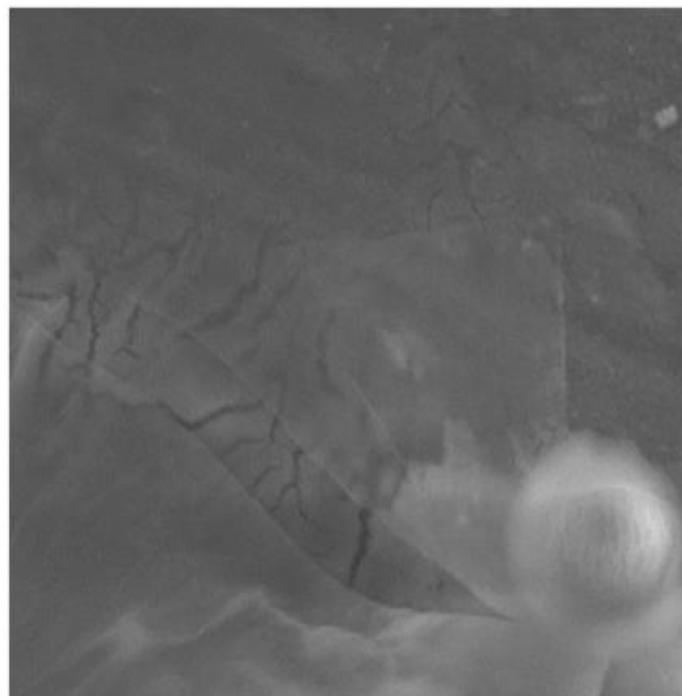
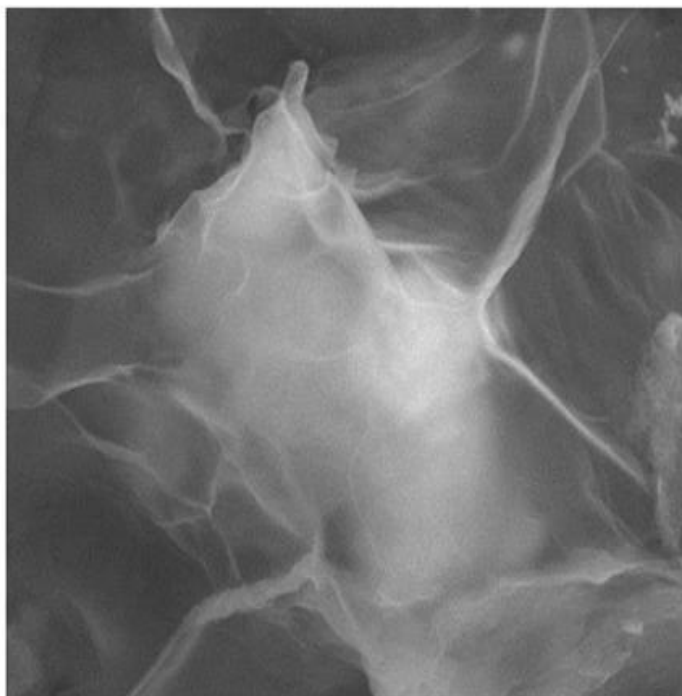


Fig. 43 SEM images of GO+4A after several washes.

Analysis with Transmission Electron microscopy were realized to verify that the layers are really thin and transparent, the diffraction showed that graphene pattern is almost preserved.

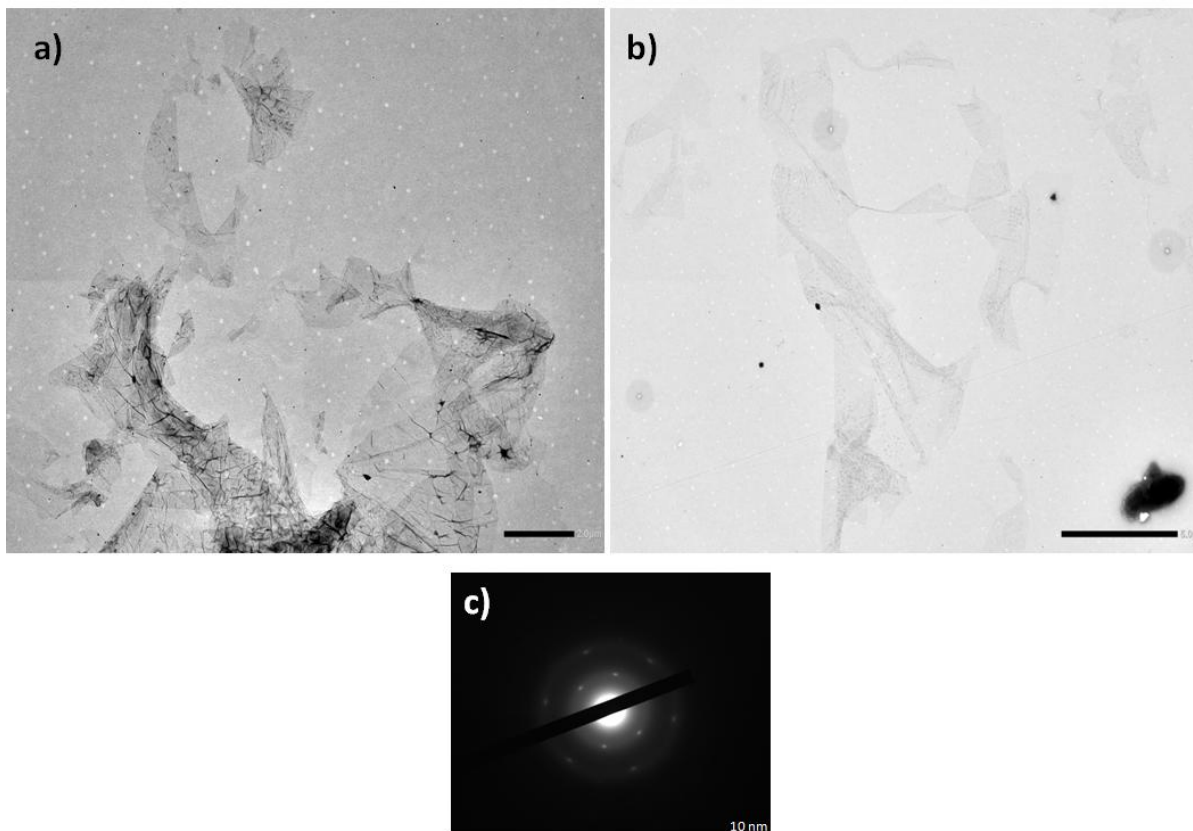


Fig. 44 TEM images of GO+4A.

The sample was diluted in water and then placed on a clean surface of tantalum as shown in Fig. 45 and this was placed in the Ultra High Vacuum system (mentioned in the first chapter).

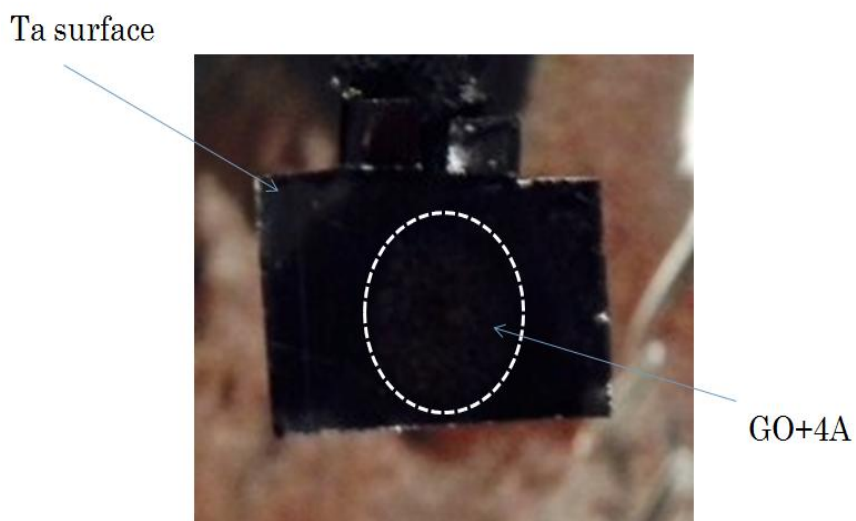


Fig. 45 Sample prepared for UHV system

XPS spectrum gives information about the composition of the sample. Strong peaks of carbon and oxygen are observed, also little peaks of Cl, S, N that that remained from the preparation of the GO. As an interesting fact, strong peaks of tantalum are observed, which confirms that the sample is really thin.

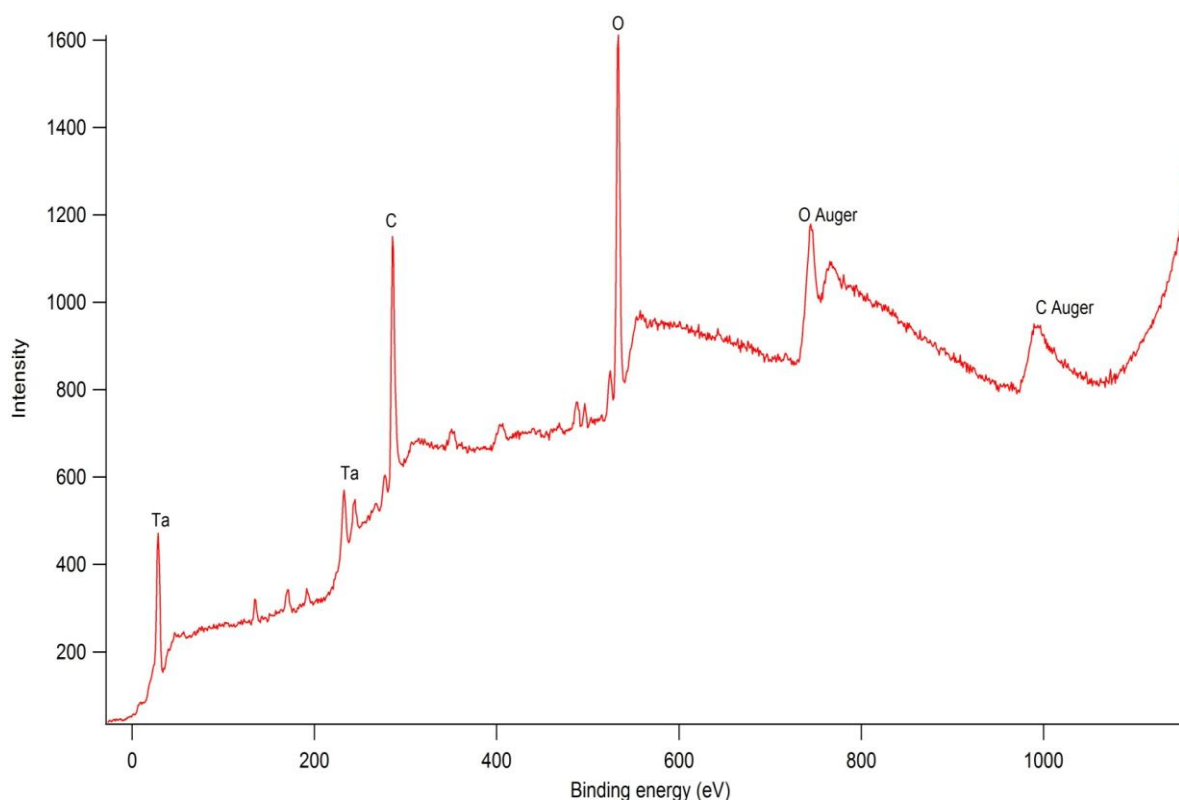


Fig. 46 XPS spectra of the GO+4A sample

This analysis evidences that there is no presence of the zeolite atoms (Si and Al), that is probably due to the large dimensions on the GO flakes. Zeolite crystals may interact with the Graphite giving energy stabilization to the flakes. For that reason there are little presence of zeolites in SEM images after the sample was diluted in 800 ml of water. However more work on this hypothesis should be realized.

Electron Energy loss spectroscopy was used in the interest to observe collective excitations in the innovative material, using as a reference the work made by Mkhoyan et al[47](See fig.47) in which a single layer of graphene oxide was measured with an EELS in transmission mode and they observe that low energy plasma excitations of  $\pi$  electrons occurs at 5 eV. In the examined case, EELS was made in reflection mode for the deposited GO+4A and  $\pi$ - Plasmon occurs at 5.8 eV as shown in the figure. The number of Graphene oxide layer in studied sample is unknown but comparing the results can be supposed that are less than 10 layers.

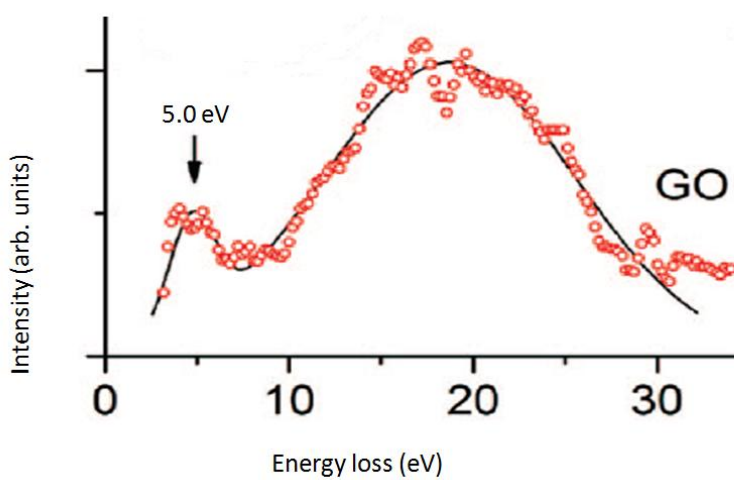


Fig. 47 Electron energy loss spectrum in the transmission mode for a single layer of Graphene Oxide[47]

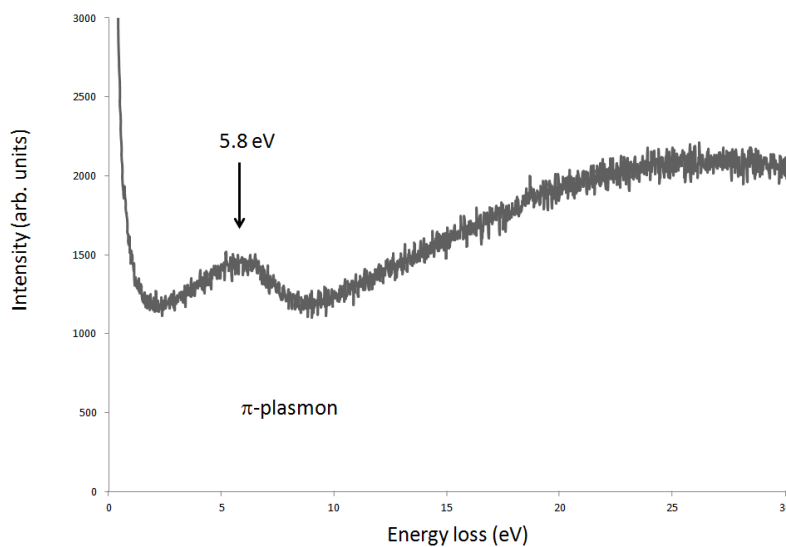


Fig. 48 EELS spectrum of GO+4A

### ***3 Final conclusions***

In this thesis, Graphene was produced by two routes: one that consisted in growing a layer of graphene onto a catalytic surface through chemical vapor deposition (CVD) and it is known as Bottom-up approach and the other used graphite as an initial material to produce graphene layers and is known as Top-down approach.

In the Bottom-up approach: the behavior of graphene grown over a nickel surface with miller index [111] was observed.

Collective electronic excitations in supported graphene are strongly affected by the underlying substrate. Can be supposed that, as graphene grown over the metal is not uniform, there are few layers distributed over the substrate leaving some space between them, and cesium could be diffused between the nickel and the graphene because it entered for the borders of the graphene.

On the assumption that cesium is in between substrate and graphene, could be explained the restitution of linearity of the graphene layer that behaves as a free-standing graphene when is well known that exist a strong interaction between graphene and the metal substrate, the presence of cesium between graphene and the nickel substrate leads to the recovering of Dirac Cones.

In the Top-down approach: graphite was mixed with some compounds as a reactant to obtain graphene. Acids were used predominantly.

As a conclusion, can be affirmed that mixing graphite only with hydrogen peroxide ( $H_2O_2$ ), or nitric acid ( $HNO_3$ ) or hydrochloride acid (HCl), does not change in an important way the structure of graphite. Even though in SEM images of the interaction with the single acids looked like it was covered from a fragmented surface, but this effect could be done for the interaction of the acids with air. Also aqua regia and graphite did not give good results. Further work should be done in this area.

Oxidation in the presence of zeolite gives very good results. Raman spectra are indicative of oxidated Graphite. EELS results obtained on graphite oxide in the reflection mode show that our GO behaves very similarly to single-layer graphene oxide. This is in agreement with our SEM and TEM results, which show very thin layers.

The reduction of GO was not included in this work. Reduction can be achieved thermal annealing, photo reduction, micro wave-assisted reduction or using chemical reduction agents (hydrazine[33] dimethylhydrazine [48] or others, there are some groups that proposed less aggressive agents such as vitamin C [49], [50] and cinnamon [51] ). In comparison with oxidation, reduction reaction is a simpler process. Oxidation is a complex process that depends of the compounds used and the preparation method, the final product is not uniform and thermally unstable[52].

The innovative introduction of zeolite in this oxidation process probably gives energetic stability to the final product, that has wide and transparent flakes. However, further work should be conducted and the potential applications of this new product should be explored.

## 4 References

- [1] J. H. Warner, F. Schaffel, M. Rummeli, and A. Bachmatiuk, *Graphene: Fundamentals and emergent applications*, vol. 17. Newnes, 2012.
- [2] H.-S. P. Wong and D. Akinwande, *Carbon Nanotube and Graphene Device Physics*. Cambridge University Press, 2011.
- [3] E. Ruiz-hitzky, M. Darder, F. M. Fernandes, E. Zatile, F. J. Palomares, and P. Aranda, "Supported Graphene from Natural Resources : Easy Preparation and Applications," pp. 5250–5255, 2011.
- [4] a H. C. Neto and K. Novoselov, "New directions in science and technology: two-dimensional crystals," *Reports Prog. Phys.*, vol. 74, no. 8, p. 082501, 2011.
- [5] a. C. Ferrari, J. C. Meyer, V. Scardaci, C. Casiraghi, M. Lazzeri, F. Mauri, S. Piscanec, D. Jiang, K. S. Novoselov, S. Roth, and a. K. Geim, "Raman Spectrum of Graphene and Graphene Layers," *Phys. Rev. Lett.*, vol. 97, no. 18, p. 187401, Oct. 2006.
- [6] A. Fonseca, S. Nejati, M. Elimelech, E. Engineering, N. Haven, and U. States, "Antimicrobial Properties of Graphene Oxide Nanosheets : Why Size Matters," no. Xx, 2015.
- [7] L. Ü. Kui, Z. Guixia, and W. Xiangke, "A brief review of graphene-based material synthesis and its application in environmental pollution management," vol. 57, no. 11, pp. 1223–1234, 2012.
- [8] Y. Cao and X. Li, "Adsorption of graphene for the removal of inorganic pollutants in water purification : a review," pp. 713–727, 2014.
- [9] N. Ligato, "Proprietà elettroniche collettive del grafene supportato : influenza del substrato."
- [10] Q. Yu, J. Lian, S. Siriponglert, H. Li, Y. P. Chen, and S.-S. Pei, "Graphene segregated on Ni surfaces and transferred to insulators," *Appl. Phys. Lett.*, vol. 93, no. 11, p. 113103, Sep. 2008.
- [11] X. Li, W. Cai, J. An, S. Kim, J. Nah, D. Yang, R. Piner, A. Velamakanni, I. Jung, E. Tutuc, S. K. Banerjee, L. Colombo, and R. S. Ruoff, "Large-area synthesis of high-quality and uniform graphene films on copper foils.," *Science*, vol. 324, no. 5932, pp. 1312–4, Jun. 2009.
- [12] J. B. Pendry, *Low Energy Electron Diffraction: The Theory and Its Application to Determination of Surface Structure*. Academic Press, 1974.
- [13] H. Raether, "Springer Tracts in modern Physics." Springer, New York, 1980.
- [14] D. Pines, "Collective energy losses in solids," *Rev. Mod. Phys.*, vol. 28, no. 3, pp. 184–198, 1956.

- [15] D. Bohm and D. Pines, "A collective description of electron interactions: III. Coulomb interactions in a degenerate electron gas," *Phys. Rev.*, vol. 92, no. 3, pp. 609–625, 1953.
- [16] R. H. Ritchie, "Plasma Losses by Fast Electrons in Thin Films," *Phys. Rev.*, vol. 106, no. 5, pp. 874–881, 1957.
- [17] A. A. Lucas and M. Šunjić, "Fast-Electron Spectroscopy of Surface Excitations," *Phys. Rev. Lett.*, vol. 26, no. 5, pp. 229–232, Feb. 1971.
- [18] E. Evans and D. L. Mills, "Theory of inelastic scattering of slow electrons by long-wavelength surface optical phonons," *Phys. Rev. B*, vol. 5, pp. 4126–4139, 1972.
- [19] E. Evans and D. L. Mills, "Oblique optical," *Phys. Rev. B*, vol. 7, no. 2, 1971.
- [20] D. L. Mills, "The scattering of low energy electrons by electric field fluctuations near crystal surfaces," *Surf. Sci.*, vol. 48, no. 1, pp. 59–79, Mar. 1975.
- [21] A. Cupolillo, N. Ligato, and L. S. Caputi, "Plasmon dispersion in quasi-freestanding graphene on Ni(111)," *Appl. Phys. Lett.*, vol. 102, no. 11, p. 111609, 2013.
- [22] T. Eberlein, U. Bangert, R. R. Nair, R. Jones, M. Gass, A. L. Bleloch, K. S. Novoselov, A. Geim, and P. R. Briddon, "Plasmon spectroscopy of free-standing graphene films," *Phys. Rev. B*, vol. 77, no. 23, p. 233406, Jun. 2008.
- [23] M. K. Kinyanjui, C. Kramberger, T. Pichler, J. C. Meyer, P. Wachsmuth, G. Benner, and U. Kaiser, "Direct probe of linearly dispersing 2D interband plasmons in a free-standing graphene monolayer," *EPL (Europhysics Lett.)*, vol. 97, no. 5, p. 57005, Mar. 2012.
- [24] M. Yi and Z. Shen, "A review on mechanical exfoliation for the scalable production of graphene," *J. Mater. Chem. A*, vol. 3, no. 22, pp. 11700–11715, May 2015.
- [25] Y. Hu, S. Song, and A. Lopez-valdivieso, "Journal of Colloid and Interface Science Effects of oxidation on the defect of reduced graphene oxides in graphene preparation," *J. Colloid Interface Sci.*, vol. 450, pp. 68–73, 2015.
- [26] Y. Hernandez, M. Lotya, D. Rickard, S. D. Bergin, and J. N. Coleman, "Measurement of multicomponent solubility parameters for graphene facilitates solvent discovery.," *Langmuir*, vol. 26, no. 5, pp. 3208–13, Mar. 2010.
- [27] F. A. de la Cruz and J. M. Cowley, "An electron diffraction study of graphitic oxide," *Acta Crystallogr.*, vol. 16, no. 6, pp. 531–534, Jun. 1963.

- [28] D. R. Dreyer, S. Park, W. Bielawski, and R. S. Ruoff, "The chemistry of graphene oxide," 2010.
- [29] J. William S. Hummers and R. E. Offeman, "Preparation of Graphitic Oxide," *J. Am. Chem. Soc.*, vol. 80, no. 1937, p. 1339, 1958.
- [30] J. Chen, B. Yao, C. Li, and G. Shi, "An improved Hummers method for eco-friendly synthesis of graphene oxide," *Carbon N. Y.*, vol. 64, no. 1, pp. 225–229, 2013.
- [31] D. C. Marcano, D. V Kosynkin, J. M. Berlin, A. Sinitskii, Z. Sun, A. Slesarev, L. B. Alemany, W. Lu, and J. M. Tour, "Improved Synthesis of Graphene Oxide," vol. 4, no. 8.
- [32] J. R. Potts, D. R. Dreyer, C. W. Bielawski, and R. S. Ruoff, "Graphene-based polymer nanocomposites," *Polymer (Guildf.)*, vol. 52, no. 1, pp. 5–25, 2011.
- [33] S. Stankovich, D. A. Dikin, R. D. Piner, K. A. Kohlhaas, A. Kleinhammes, Y. Jia, and Y. Wu, "Synthesis of graphene-based nanosheets via chemical reduction of exfoliated graphite oxide," vol. 45, pp. 1558–1565, 2007.
- [34] Q. Bao, D. Zhang, and P. Qi, "Journal of Colloid and Interface Science Synthesis and characterization of silver nanoparticle and graphene oxide nanosheet composites as a bactericidal agent for water disinfection," *J. Colloid Interface Sci.*, vol. 360, no. 2, pp. 463–470, 2011.
- [35] W. Virginia, "Trends and Frontiers in Graphene-Based Polymer," no. January, pp. 32–43, 2011.
- [36] L. Sun and B. Fugetsu, "Graphene oxide captured for green use: Influence on the structures of calcium alginate and macroporous alginic beads and their application to aqueous removal of acridine orange," *Chem. Eng. J.*, vol. 240, pp. 565–573, Mar. 2014.
- [37] J. Guerrero-contreras, "Graphene oxide powders with different oxidation degree , prepared by synthesis variations of the Hummers method," *Mater. Chem. Phys.*, vol. 153, pp. 209–220, 2015.
- [38] H. Raza, *Graphene Nanoelectronics: Metrology, Synthesis, Properties and Applications*. Springer Science & Business Media, 2012.
- [39] D. R. Dreyer, A. D. Todd, and C. W. Bielawski, "Harnessing the chemistry of graphene oxide," *Chem. Soc. Rev.*, vol. 43, no. 15, p. 5288, 2014.
- [40] P. A. Jacobs, E. M. Flanigen, J. C. Jansen, and H. van Bekkum, *Introduction to Zeolite Science and Practice*. Elsevier, 2001.
- [41] I. T. O. Zeolites, "Zeolites: A Primer," 2003.
- [42] H. Lüth, *Surfaces and Interfaces of Solid Materials*. Springer Science & Business Media, 2013.

- [43] "Wiley: Raman Spectroscopy in Graphene Related Systems - Ado Jorio, Mildred S. Dresselhaus, Riichiro Saito, et al." [Online]. Available: <http://eu.wiley.com/WileyCDA/WileyTitle/productCd-3527408118.html>. [Accessed: 03-Dec-2015].
- [44] A. Ambrosi, C. Kiang, B. Khezri, R. D. Webster, and M. Pumera, "Chemically reduced graphene contains inherent metallic impurities present in parent natural and synthetic graphite," vol. 109, no. 32, pp. 12899–12904, 2012.
- [45] D. C. Fiallos, C. V. Gómez, G. T. Usca, D. C. Pérez, P. Tavolaro, G. Martino, L. S. Caputi, and A. Tavolaro, "Removal of acridine orange from water by graphene oxide," in *INTERNATIONAL CONFERENCES AND EXHIBITION ON NANOTECHNOLOGIES AND ORGANIC ELECTRONICS (NANOTECHNOLOGY 2014): Proceedings of NN14 and ISFOE14*, 2015, vol. 1646, no. 1, pp. 38–45.
- [46] J. Chen, Y. Li, L. Huang, C. Li, and G. Shi, "High-yield preparation of graphene oxide from small graphite flakes via an improved Hummers method with a simple purification process," *Carbon N. Y.*, vol. 81, pp. 826–834, Jan. 2015.
- [47] K. A. Mkhoyan, A. W. Contryman, J. Silcox, D. A. Stewart, G. Eda, C. Mattevi, and S. Miller, "Atomic and Electronic Structure of Graphene-Oxide," pp. 17–21, 2009.
- [48] S. Stankovich, R. D. Piner, S. T. Nguyen, and R. S. Ruoff, "Synthesis and exfoliation of isocyanate-treated graphene oxide nanoplatelets," vol. 44, pp. 3342–3347, 2006.
- [49] L. Guardia, J. I. Paredes, P. Soli, and J. M. D. Tasco, "Vitamin C Is an Ideal Substitute for Hydrazine in the Reduction of Graphene Oxide Suspensions," pp. 6426–6432, 2010.
- [50] S. Rella, A. Giuri, C. Esposito, M. Rosaria, S. Colella, G. Guerra, A. Listorti, A. Rizzo, and C. Malitesta, "X-ray photoelectron spectroscopy of reduced graphene oxide prepared by a novel green method," *Vaccum*, vol. 119, pp. 159–162, 2015.
- [51] D. Suresh, M. A. Pavan Kumar, H. Nagabhushana, and S. C. Sharma, "Cinnamon supported facile green reduction of graphene oxide, its dye elimination and antioxidant activities," *Mater. Lett.*, vol. 151, pp. 93–95, Jul. 2015.
- [52] S. Stankovich, D. A. Dikin, R. D. Piner, K. A. Kohlhaas, A. Kleinhammes, Y. Jia, Y. Wu, S. T. Nguyen, and R. S. Ruoff, "Synthesis of graphene-based nanosheets via chemical reduction of exfoliated graphite oxide," *Carbon N. Y.*, vol. 45, no. 7, pp. 1558–1565, Jun. 2007.
- [53] Kittel, *Introduction to solid state physics*. Wiley India Pvt. Limited, 2007.
- [54] M. I. Katsnelson and M. I. Katsnel'son, *Graphene: Carbon in Two Dimensions*. Cambridge University

Press, 2012.

- [55] *Graphite, Graphene, and Their Polymer Nanocomposites*. CRC Press, 2012.
- [56] S. Sen Gupta, T. S. Sreepasad, S. M. Maliyekkal, S. K. Das, and T. Pradeep, "Graphene from Sugar and its Application in Water Purification," 2012.
- [57] I. N. Levine, *Molecular spectroscopy*. Wiley, 1975.
- [58] R. Nagarjuna, S. Challagulla, N. Alla, R. Ganesan, and S. Roy, "Synthesis and characterization of reduced-graphene oxide / TiO<sub>2</sub> / Zeolite-4A : A bifunctional nanocomposite for abatement of methylene blue," *JMADE*, vol. 86, pp. 621–626, 2015.
- [59] a. Cupolillo, N. Ligato, and L. S. Caputi, "Two-dimensional character of the interface-?? plasmon in epitaxial graphene on Ni(1 1 1)," *Carbon N. Y.*, vol. 50, no. 7, pp. 2588–2591, 2012.

## ***Publications***

- Cupolillo, A. Politano, N. Ligato, D. M. C. Perez, G. Chiarello, and L. S. Caputi, “Surface Science Substrate-dependent plasmonic properties of supported graphene Intensity [ Arb . Units ],” *Surf. Sci.*, vol. 634, pp. 76–80, 2015.
  
- D. C. Fiallos, C. V. Gómez, G. T. Usca, D. C. Pérez, P. Tavoraro, G. Martino, L. S. Caputi, and A. Tavoraro, “Removal of acridine orange from water by graphene oxide,” in *INTERNATIONAL CONFERENCES AND EXHIBITION ON NANOTECHNOLOGIES AND ORGANIC ELECTRONICS (NANOTECHNOLOGY 2014): Proceedings of NN14 and ISFOE14, 2015*, vol. 1646, no. 1, pp. 38–45.

## ***Acknowledgments***

**“Giving thanks always for all things unto God and the Father**

**in the name of our Lord Jesus Christ”**

Ephesians 5:20

Thanks to God for giving me the strength, energy and dedication necessary to achieve this goal.

To my advisors: Prof. Lorenzo S. Caputi and Dott.ssa Adalgisa Tavolaro: Thanks For all the patient and supporting me every time.

I want thank my parents: Mirian Perez and Felix Cid, my brother Felix Antonio, my aunt Denia, to my uncles (Allendi, Eduard, Jose Ramon, Milton, Moises, Ruddy, Praede, Alcibiades) and aunts (Agustina, Rosaliness and Geisa), my cousins (specially Miguel, Melissa, Nasla, Oliver and Lily) and my Grandmother for their support at all times.

I would like to thanks specially the Professor Galileo Violini that was person that informed me about this opportunity and helps me every time. It is an exceptional human being and an example of inspiration. I would like to thanks his family too.

To my teachers: Dra. Anna Cupolillo, Dr. Melvin Arias and Ramón de Jesús Núñez Laurens (Papito).

To Dra. Claudia Giallombardo and Dra. Nadia Ligato, I learned a lot of things from you.

To my friends and colleagues: Katelyne, Mariella, Nelphy, Aneika, Evelin, Marco , Gaby (H), Gaby (E) , Marco P, Mirna, Fanny, Eduardo, Elena, Rosibella, Pris Killa, Marlon, Salih, Serena, Emanuelle, Vlorá, Francesco (Narda), Vesarta, Domenico, Angela, Jacopo, Diana, Mario, Dianita (Hola enfermera!), Jorge, Citra, Lucas, Tabita, Alessandro, Margarita, Paolo, Ting, Tarteel, Marlon, Salih, Teresa, Lazare, Santina, Ivana, Airama, Leo, Yairis, Andrea, Pauly, Sergio, Sara and Rosalia .

I would like to thank again to my Professor again and his wife Arianna, Doña Rita, Giulia and all members of Caputi’s family that received me as a member of their family.

To Pastor Marco and his wife Verena, Carla and Raimondo, Marcia and her family , Giovanni, Tina, Annamaria and all the members of Siloe church, you are like a family for me.

In the end, but not less important, I would like to thank to Dra. Daniella Perrota from TEM, Dra. Rafaella De Luca from Raman and Dr. Mariano Davoli from SEM.

This work is dedicated to all those who have contributed in some way to make this goal a reality. I have no words to express all my gratitude. Thank you so much.